



Dual-defect enhanced piezocatalytic performance of C_3N_5 for multifunctional applications

Cheng Fu, Tao Wu, Guowei Sun, Guofeng Yin, Chan Wang, Guoxia Ran, Qijun Song^{*}

Key Laboratory of Synthetic and Biological Colloids, Ministry of Education, School of Chemical and Material Engineering, Jiangnan University, 1800 Lihu Road, Wuxi, Jiangsu Province 214122, PR China

ARTICLE INFO

Keywords:

C_3N_5
Defect engineering
Piezocatalytic degradation
Piezocatalytic H_2O_2 production
Piezocatalytic Fenton

ABSTRACT

An effective piezocatalytic semiconductor ($C_3N_{5-x}O$) was prepared with a two-step thermal polymerization/etching method. Experimental characterizations and structural simulations revealed that the dual-defects of O doping and N vacancy in C_3N_5 not only increases the asymmetry and the exposure of triangular pores, but also optimizes the band structure and charge distribution of the thin-layered $C_3N_{5-x}O$, endowing it with an enhanced piezoelectricity and increased active surfaces. Piezocatalysis-mediated pollutant degradation and H_2O_2 production were achieved with substantially improved efficiencies over the pristine carbon nitrides. Under ultrasound-assisted piezocatalysis, tetracycline was degraded with a kinetic rate of 0.0356 min^{-1} and this figure was further increased to 0.0561 min^{-1} in piezocatalytic-Fenton. A yield of 0.615 mM/g/h for piezocatalytic production of H_2O_2 was achieved in pure water. The synergistic effect of the defect sites revealed in present work could facilitate the more rational design of nitrogen-rich carbon nitrides for environmental remediation and the production of value-added chemicals.

1. Introduction

Piezocatalysis is an environmentally friendly method to alleviate environmental pollution and produce value-added chemicals [1–4]. Under external mechanical stress or strain conditions, the ordered accumulation of the dipole moments produced in the unit cells of catalysts can generate piezopotential to separate and transfer the charge carriers to the surface of catalyst for generating free radicals and H_2O_2 [5]. Meanwhile, since mechanical energies widely exist in nature, such as muscle movement, tides, rivers, and wind, the piezoelectric effect induced by the mechanical energies should be a promising strategy for wastewater treatment and the production of H_2O_2 with pure water [2,6,7]. However, the practical applications of most semiconductor piezocatalysts are often restricted by their insufficient piezoelectric polarization, limited active sites, and small energy collection areas. As a successful tactic, defect engineering has appeared to be an effective and simple approach to improving piezocatalytic performance of catalysts [6,8–11]. For example, the existence of oxygen vacancies in $BaTiO_3$ and $Bi_4Ti_3O_{12}$ enhances the piezoelectric nature and O_2 activation [9,12]. However, many reported studies so far have focused on the enhancement in piezoelectricity of catalyst, such as the piezoelectric potential

[5], but overlooked the subsequent chemical processes on the catalyst surface. The chemical processes, such as the adsorption behavior of reactive substrates, the charge transfer after adsorption, and the reaction pathway in the catalytic process are also important factors for the overall performance of a piezocatalyst.

It is generally recognized that an optimum piezocatalyst should have a thin 2D structure with a large BET value, a high ratio of surface atoms, and a high piezoelectric coefficient [13–15]. Additionally, the surface chemical process benefits more from the exposure of active sites. Examples of materials with strong piezocatalytic performance include few-layered ZnS_2 and MoS_2 , which profit from their high piezoelectric potential and abundance of reactive sites [16,17]. However, these metal-based catalysts cause great concern when they are used for environmental treatment or H_2O_2 production, so employing metal-free catalysts is more environmentally friendly. Tiny triangular-shaped holes or polar groups can be inserted into graphene to produce the asymmetric charge density distribution and enhance the piezocatalytic performance of carbon-based nanomaterials [15]. An earlier study found that N-doped graphene combined with MoC quantum dots performed well for piezocatalytic H_2 evolution due to the enhanced piezoelectric potential [18]. As a kind of traditional carbon material,

^{*} Corresponding author.

E-mail address: qsong@jiangnan.edu.cn (Q. Song).

<https://doi.org/10.1016/j.apcatb.2022.122196>

Received 15 August 2022; Received in revised form 14 November 2022; Accepted 16 November 2022

Available online 17 November 2022

0926-3373/© 2022 Elsevier B.V. All rights reserved.

C_3N_4 is also a promising semiconductor for piezocatalysis and photocatalysis [19,20]. C_3N_4 with few-layered structures and optimized defects possess better piezocatalytic and/or photocatalytic activities than pristine C_3N_4 [15,19,21,22]. Strong in-plane polarization and flexoelectricity are produced in the triazine plane of C_3N_4 due to the presence of triangular-shaped nanoholes in the layers [23]. Importantly, piezoelectricity also appears in the bulk phase of C_3N_4 , unlike MoS_2 , which exhibits strong piezoelectric polarization only in odd layers [24]. Compared to C_3N_4 , nitrogen-rich carbon nitrides (such as C_3N_5 , C_3N_6 , and C_3N_7) are newly emerged semiconductors with triazine and/or triazole units, thus they could have a more attractive photo/electrocatalytic activity [25–31]. However, the piezocatalytic performance of these materials has not been exploited so far. It is therefore very encouraging to investigate and optimize piezocatalytic properties of nitrogen-rich carbon nitrides for the piezocatalytic degradation of organic pollutants and H_2O_2 production. Based on these considerations, C_3N_5 was selected as an example for the subsequent study.

In the present work, a thermal polymerization combined thermal etching approach was used to effectively produce dual-defect C_3N_5 containing O doping and N vacancies. The superior piezocatalytic performance of C_3N_5 over C_3N_4 is shown for the first time, and defect engineering can further enhance piezocatalytic degradation, Fenton, and H_2O_2 production. It was found that thermal etching helps to form thin-layer and porous structures, exposing more triangular pores to increase piezoelectric nature. And defect engineering also effectively enhances the asymmetry of the molecular structure of the catalyst to increase the polarization and piezoelectric properties [2]. The finite element method (FEM) simulation and the piezoresponse force microscopy (PFM) were used to characterize the piezoelectricity of the catalyst. Density functional theory (DFT) calculations also revealed that the catalyst with the dual-defect sites has an optimized surface electronic structure, which facilitates the subsequent surface chemical process. Consequently, the piezocatalytic system of $C_3N_{5-x}O$ can effectively degrade tetracycline (TC) and rhodamine B (RhB) under ultrasound assistance, and the degradation efficiency was further increased in the piezocatalytic Fenton system. Significantly, the piezocatalytic system has shown an excellent performance even in the presence of high background ions or high levels of contaminants, demonstrating its great potential in practical application. Furthermore, a yield of H_2O_2 as high as 0.615 mM/g/h

was obtained by the piezocatalytic reduction of O_2 without the addition of any sacrifice agent. Finally, the mechanism for the piezocatalytic degradation and H_2O_2 production is comprehensively investigated.

2. Experiment

Chemicals, control sample synthesis, characterization methods, experimental methods of degradation, and computational framework, are detailed in [Supporting Information](#). In addition, the symbols of the control samples are summarized as follows: C_3N_5 (pristine C_3N_5), C_3N_5-O (C_3N_5 with O site), C_3N_{5-x} (C_3N_5 with N vacancy), C_3N_4 (pristine C_3N_4), $C_3N_{4-x}O$ (dual-defect C_3N_4).

2.1. Synthesis of dual-defect C_3N_5 ($C_3N_{5-x}O$)

In a typical procedure, an amount of 1 g 3-amino-1,2,4-triazole and 4.4 mmol oxalic acid were polymerized in an Ar atmosphere at 500 °C for 3 h with a ramp rate of 5 °C/min. Only by changing the gas atmosphere, 0.5 g of the product was subjected to re-pyrolysis under the open atmosphere to obtain the $C_3N_{5-x}O$ precursor. The precursors were collected and sonicated for 30 min, then washed three times with ultrapure water, and finally vacuum dried at 60 °C to obtain $C_3N_{5-x}O$. And a schematic diagram of the synthesis process is summarized in [Fig. 1](#).

3. Results and discussion

3.1. The characterization of C_3N_5 -based catalysts

C_3N_5 is an emerging semiconductor that can be obtained by thermally polymerizing 3-amino-1,2,4-triazole and is considered to have higher photocatalytic and electrocatalytic properties than traditional C_3N_4 [25–28]. To further explore and optimize the piezocatalytic properties of C_3N_5 , we constructed a series of C_3N_5 -based catalysts with different defects. Next, we focus on the dual-defect C_3N_5 with the highest piezocatalytic performance. In [Fig. 1a](#), a schematic representation of the two-step synthesis of dual-defect C_3N_5 (denoted as $C_3N_{5-x}O$) is presented, along with the changes in microscopic morphology ([Fig. 1b, c](#), and [Fig. S1](#)) of primary C_3N_5 and single-defect C_3N_5 .

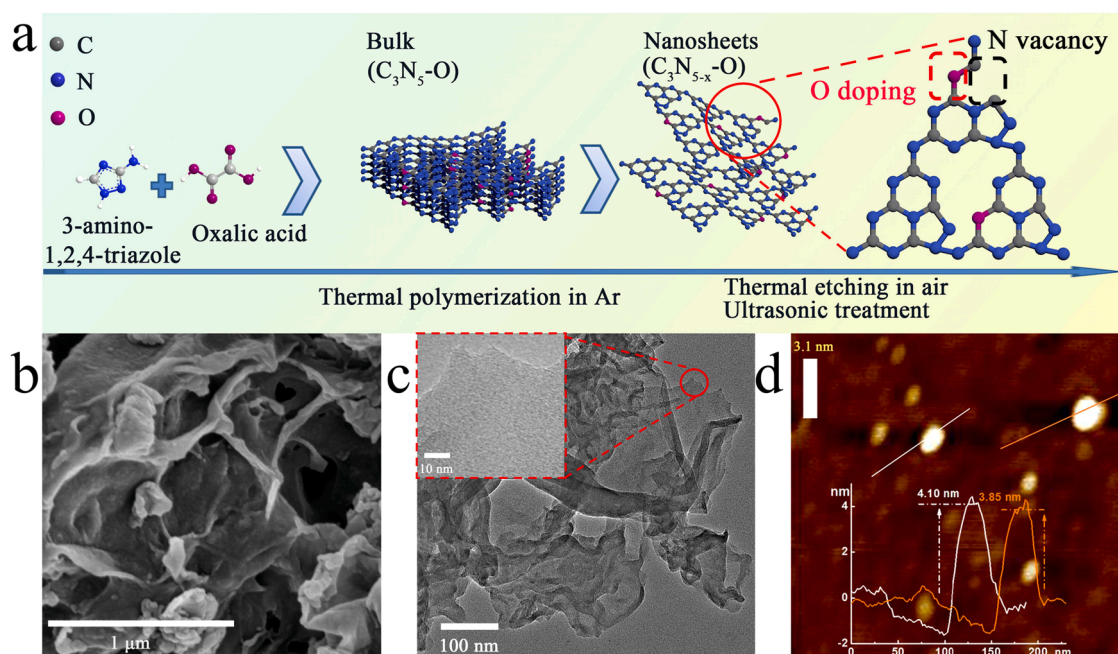


Fig. 1. (a) the synthetic route, (b) SEM image, (c) TEM image, (d) AFM image and corresponding height curves (inset) of $C_3N_{5-x}O$.

Furthermore, atomic force microscopy (AFM) analysis reveals that even the flake scraped from pristine C_3N_5 has a thickness of around 32 nm (Fig. S2), while the thickness of $C_3N_{5-x}O$ reduces to about 4 nm, including roughly ten atomic layers (Fig. 1c). In addition, the TEM mapping data confirmed the uniform distribution of C, N, and O (Fig. S1 d-g).

X-ray diffraction (XRD) was used to reveal the structures of all the materials. As illustrated in Fig. 2a, C_3N_5 -based materials have two distinct peaks at 13.4° and 27.7° , allocated to the (100) and (002) planes, which indicate in-plane structural ordering and interlayer stacking, respectively [28]. Different from C_3N_5 -based materials, the (100) and (002) planes of C_3N_4 -based materials were 13.1° and 27.4° , which can be attributed to the difference in in-plane packing and interlayer stacking, respectively. The two diffraction peaks were diminished significantly after re-pyrolysis of C_3N_5 -O, suggesting that this thermal etching strategy formed defects in pristine C_3N_5 structural units and hindered multilayer stacking. According to the formation energy data (Fig. S3 and Table S1), the 4_N site in the triazine unit of C_3N_5 is the most likely to produce N vacancy. Strong in-plane polarization and flexoelectricity are produced in the triazine plane of C_3N_4 due to the presence of triangular-shaped nanoholes in the layers [23]. Similarly, $C_3N_{5-x}O$ with a triangular structure should also have higher piezoelectric nature than the structurally broken $C_3N_{5-x}O$. Combined with the formation energy data of dual-defect C_3N_5 , it can be considered that the 4_N and 5_N sites are N vacancy and O doping, respectively.

The characteristics of chemical bond in C_3N_5 -based materials and C_3N_4 -based materials are comparatively demonstrated in the Fourier-transform infrared (FT-IR) spectra (in Fig. 2b). The weak peaks at 891 and 810 cm^{-1} can be ascribed to the condensed C-N heterocycles of the triazine moiety [25], which are lower in C_3N_5 -based materials than that of C_3N_4 -based materials, suggesting the existence of a lower number of C-N bonds. Comparing with that of pristine C_3N_5 , the characteristic peaks of triazine moiety were further decreased in the defect C_3N_5 , suggesting that the defects are created during the loss of the triazine moiety. The assumption was also supported by the formation energy data (Fig. S3 and Table S1). In carbon nitride based materials, N-H stretching vibrations are responsible for the several wide peaks in the 3000–3500 cm^{-1} range [32]. $C_3N_{5-x}O$ had a considerable drop in the intensity of the N-H stretching vibration after C_3N_5 was re-pyrolysis in

the air atmosphere. According to these results, it is evident that the two-step defect procedure reduces the content of N-H groups and facilitates the creation of nitrogen vacancies.

Element analysis and X-ray photoelectron spectroscopy (XPS) were conducted to elucidate the elemental composition and the defect state of C_3N_5 -based materials. The atomic ratios of C/N, C/H, and C/O in C_3N_5 before and after defect engineering are shown in Table S2. The increase in C/N value is related to the existence of N vacancies. The increase in the C/H atomic ratio indicates the loss of H, which is consistent with the drop in the N-H characteristic peak in the FTIR data. The drop in the C/O value indicates the successful doping of O atoms. Furthermore, the high-resolution C 1s (Fig. 2c), O 1s (Fig. 2d), and N 1s (Fig. 2e) spectra reveal more details regarding the defect states and valence state of elements. The strong peak at 288.1 eV in the C 1s spectra of C_3N_5 and C_3N_5 -O (Fig. 2c) corresponds to the N=C-N group, whereas the peak at 284.6 eV is assigned to adventitious C [28]. The C-NH₂ group is responsible for the third peak at 288.9 eV [28]. The new peaks located at 286.1 eV and 287.3 eV in C_3N_5 -O and $C_3N_{5-x}O$ belong to the C-O bond in ether or hydroxyl groups and carbonyl groups (C=O) [33]. Except for the common peaks for adsorbing water (532.1 eV) and oxygen (533.5 eV) molecules, the additional peak in the O1s spectra at 531.2 eV shows C-O/C=O [34], which is consistent with the C1s results. The peaks at 398.7 eV and 400.1 eV in the high-resolution N 1s spectrum are attributed to the C-N-C group and bridging nitrogen atoms (C-N=N-C) or amino groups (C-NH₂), revealing the presence of triazine and triazole moiety in all C_3N_5 -based materials [26,28,35]. Table S3 shows the proportions of several N species. The peak intensities of C-N-C in dual-defect and single-defect C_3N_5 -based materials are much lower than in pristine C_3N_5 , showing that defect engineering eliminates part of the triazine structure, which is compatible with formation energy and FTIR data. In addition, the two weak peak at C 1s (293.3 eV) and N 1s (404.7 eV) can be attributed to the delocalization of π electron, indicating graphitic stacking in all C_3N_5 -based materials [26,36].

Because defect engineering could alter the electronic structure of materials, electron paramagnetic resonance (EPR) was utilized to determine the link between unpaired electrons and defect states [37,38]. As seen in Fig. 2f, $C_3N_{5-x}O$ has a higher Lorentzian signal (g-factor, 2.003) than pristine C_3N_5 , showing that O doping and N vacancy help to produce more unpaired electrons. When investigating the probable

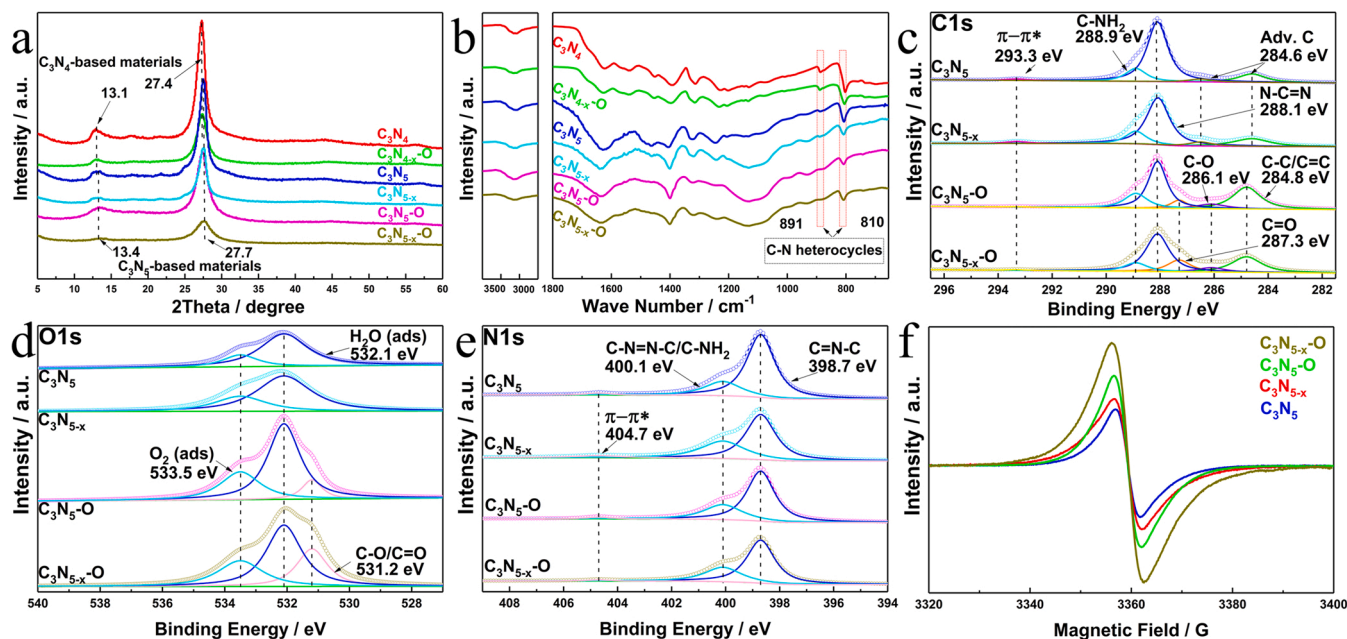


Fig. 2. (a) XRD patterns and FTIR spectra (b) of all catalysts. (c) C 1s XPS, (d) O 1s XPS, and (e) N 1s XPS of all C_3N_5 -based catalysts. (f) EPR spectra of C_3N_5 -based materials.

sources of charge carriers in piezocatalysis, the intrinsic unpaired charges originating from defects cannot be ignored [39,40]. The goal of defect engineering is to increase the concentration of free charges to improve piezocatalytic activity [5], which is also in line with the experimental fact that defect engineering improves piezocatalytic activity in this work.

The redox ability of a semiconductor is determined by the location of the conduction band (CB) and valence band (VB) [6]. However, a wide energy gap is a restriction for potential-driven electron transport and subsequent catalytic reactions [41,42]. UV-vis diffuse reflectance spectra (DRS) were used to explore the electronic structures (Fig. 3a). After defect engineering, the absorption bands originated from the $\pi-\pi^*$ electronic transition were amplified, whereas additional absorption bands derived from the $n-\pi^*$ electronic transition of the lone pair of electrons at defect sites emerged [43–45]. Similar to the EPR data, defect engineering has optimized the electronic structure of the catalyst. The band gap of the C_3N_5 -based materials shrunk from 1.98 to 1.78 eV (Fig. S4), as seen by the translated Kubelka–Munk function, which is consistent with the trend of computed band structures (Fig. 3b, c). In addition, the charge density distributions of C_3N_5 and $C_3N_{5-x}O$ for the primary energy bands (VBM-1, VBM, CBM, and CBM+1) are shown in Figs. 3g and 3h. The dual-defect sites result in a spatial re-distribution of charge density that facilitates the subsequent polarization enhancement, carrier separation, and catalytic activity [46]. The photoluminescence

(PL) intensity of C_3N_5 was reduced by defect engineering, implying that the dual-defect sites efficiently promoted carrier separation (Fig. 3d). Carrier separation efficiency is another key factor for piezocatalytic performance. And, the carriers excited by mechanical energy may also be easier to separate on the dual-defect C_3N_5 and participate in the subsequent chemical reactions. To directly investigate the piezoelectric response of the materials, electrochemical impedance spectroscopy (EIS) and transient current response experiments were conducted. As can be seen from Fig. 3e, ultrasonic treatment has little effect on impedance reduction in the absence of catalysts, whereas in the presence of a catalyst the impedance dropped dramatically under ultrasound vibration. Presumably, the catalyst could act as tiny cells under ultrasonic-induced stress, leading to the improvement in the conductivity of suspension [47]. And this phenomenon is more pronounced after defect engineering, showing that defect engineering improves the piezoelectric response. Furthermore, the transient current response data also backs up this point (Fig. 3f). To further investigate the band structure, MottSchottky plots were used to find out the flat band (Fig. S5 a, b) [48]. Due to the positive slopes of the curves, C_3N_5 and $C_3N_{5-x}O$ are typical n-type semiconductor. The flat band of C_3N_5 and $C_3N_{5-x}O$ are -0.96 V and -1.03 V. After the calculation, the CB of C_3N_5 and $C_3N_{5-x}O$ are estimated to be -0.72 V and -0.79 V, respectively. So the VB positions of C_3N_5 and $C_3N_{5-x}O$ are around 1.26 V and 0.88 V. Open-circuit voltage decay (OCVD) was used to investigate dynamic of

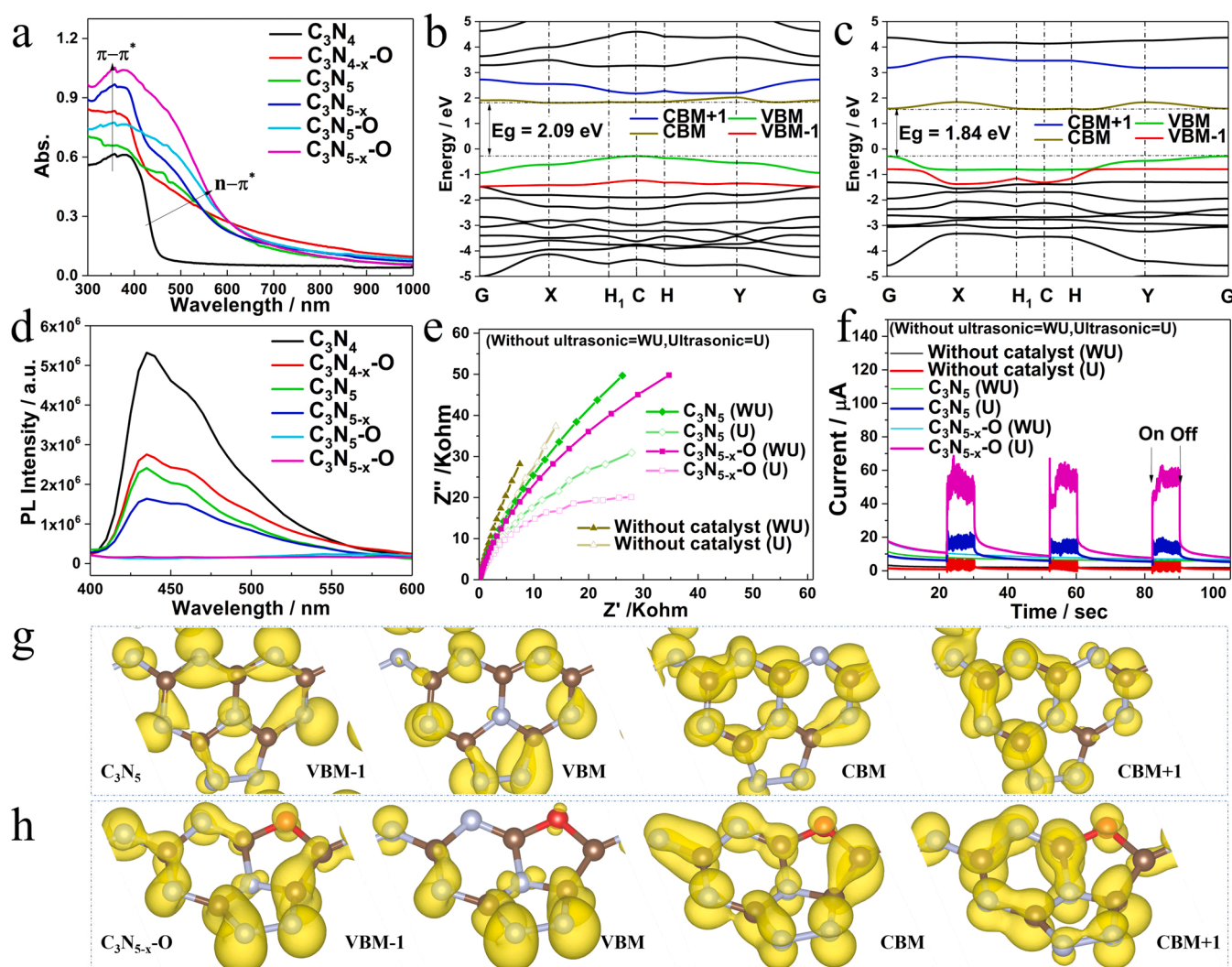


Fig. 3. (a) UV-vis DRS and (d) PL spectra of all the catalysts. The band structure of (b) C_3N_5 and (c) $C_3N_{5-x}O$. (e) EIS and (f) transient current response of $C_3N_{5-x}O$ and pristine C_3N_5 . The charge density distribution of VBM-1, VBM, CBM, CBM+ 1 in (g) C_3N_5 and (h) $C_3N_{5-x}O$.

piezocarriers (Fig. S5 c). Almost consistent curves imply that defect engineering has less impact on carrier lifetime.

Based on UV-vis DRS, fluorescence, electrochemistry, EPR, and charge distribution data, it is reasonable to conclude that defect engineering optimizes the electronic structure for increased polarization and effective carrier separation under the piezoelectric field.

3.2. Piezocatalytic performance of catalysts

3.2.1. Piezocatalytic degradation

To investigate the piezocatalytic properties of different catalysts, we first established a series of degradation systems initially using RhB as the model substrate. According to Fig. 4a and Fig. S6, C_3N_5-x-O has the best piezocatalytic performance, completely degrading 20 ppm of RhB in 40 min with a kinetic constant of 0.0965 min^{-1} . This result indicates

that the dual-defect C_3N_5 is more effective in the piezocatalytic performance than that of single-defect C_3N_5 or pristine C_3N_5 . When the conventional C_3N_4 was modified with dual-defects, its piezocatalytic degradation rate for RhB increased from 62.8% to 73.5%, but these figures are still significantly less than that obtained from C_3N_5 -based materials. Additionally, the degradation rate of RhB is only 7.7% in the absence of a catalyst, and the kinetic constant value is 0.0019 min^{-1} , demonstrating the critical function of the catalysts. Furthermore, oxygen sites are more effective in the improvement of piezocatalytic performance compared to that the N vacancies, which is also supported by the DFT results (Table S4). In comparison to catalysts containing N vacancies, catalysts with O sites exhibit higher O_2 adsorption energy, longer O-O bonds, and more electron transfer between the catalyst and O_2 , resulting in a strong O_2 activation capacity [32]. Similarly, the data in Table S4 also explain why C_3N_5-x-O has stronger piezocatalytic

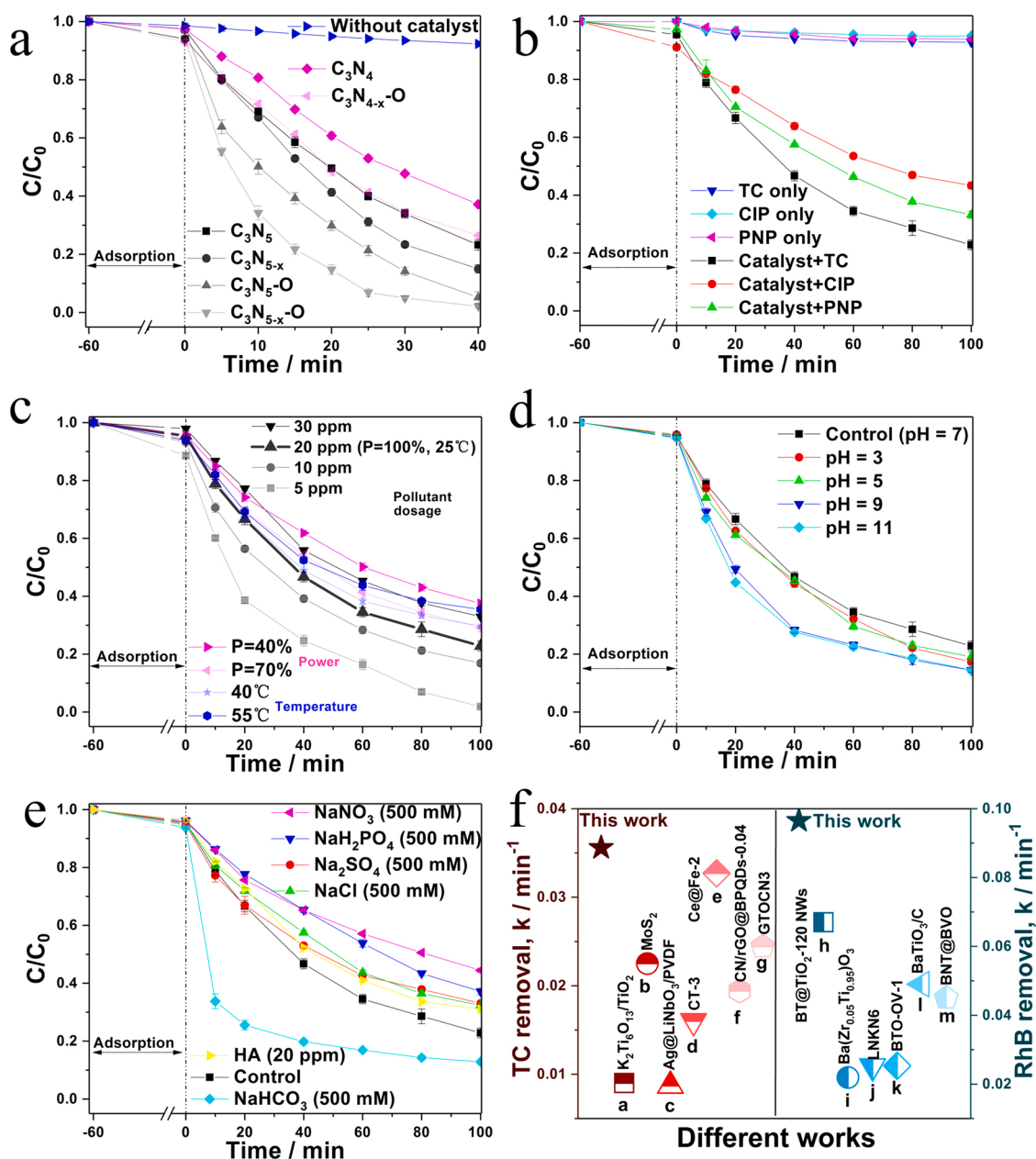


Fig. 4. (a) Piezocatalytic degradation performances of prepared catalysts for piezodegradation of 20 ppm RhB. (b) Degradation curves for various refractory pollutants (20 ppm) with C_3N_5-x-O . (c) Degradation curves of TC under different parameters, including dosage, power, and temperature. (d) Degradation curves of 20 ppm TC under different pH by C_3N_5-x-O . (e) Degradation curves of 20 ppm TC under different interference conditions, including frequently encountered inorganic substances and organic macromolecules. (f) Comparison of reaction kinetic constants in this work with other literatures.

properties than that $C_3N_{4-x}O$.

Various contaminants were used to study the practical applicability of $C_3N_{5-x}O$ in piezocatalytic degradations. Fig. 4b shows that the degradation rates for 20 ppm TC, CIP, and PNP were all less than 10% in 100 min ultrasound treatment without the addition of catalysts. In contrast, the degradation rates increase to 77.2%, 56.7%, and 66.8%, respectively for TC, CIP, and PNP in the presence of $C_3N_{5-x}O$. The degradation conditions were further investigated by using TC as the model substrate. TC is a frequently used broad-spectrum antibiotic in both biomedicine and aquaculture. It is a refractory pollutant and has a detrimental effect to biodegradation techniques, hence its piezocatalytic degradation is more meaningful in water treatment. Fig. 4c and Fig. S7 show the dependence of the degradation rate on the mass ratio of catalyst to TC. Complete degradation of 5 ppm TC was achieved in 100 min with the mass ratio of catalyst to TC is 100. The decomposition of TC is an endothermic reaction, however, it was found that the increase of temperature is not conducive to the degradation, which could be attributed to the unfavorable dissolution of oxygen and the subsequent generation of ROS in increased temperatures [49,50]. As shown in Fig. 4d, the efficient degradation of TC can be achieved in a wide pH range (3–11). In alkaline conditions, the degradation rate was slightly greater, presumably because TC is less stable in alkaline conditions (Fig. S8a) [51,52]. On the other hand, this can be attributed to the easier deprotonation of piezocatalytically formed H_2O_2 in alkaline condition and subsequent conversion to ROS [53]. After accounting for pH influence, we further calculate the real kinetic constant ($k_{real} = k_{with\ catalyst} - k_{without\ catalyst}$). It was found that the piezocatalytic degradation system has the greatest degradation performance in alkaline condition, which agree well with the experiment data (Fig. S8b). TOC data further supports this conclusion (Fig. S9). Thus a high degradation kinetic constants of $0.0356\ min^{-1}$ for TC and $0.0965\ min^{-1}$ for RhB were obtained with the $C_3N_{5-x}O$ piezocatalyst, which is among the best performance of reported catalysts (Fig. 4f) [7,9,54–64].

The practical use of piezocatalytic systems was investigated by simulating water with the addition of frequently encountered inorganic substances and organic macromolecules. Figs. 4e and S10 show that up to 10 ppm of inorganic substances have a negligible effect on TC degradation. It is noted that only up to 500 ppm inorganic compounds can exhibit a relatively high inhibition on the TC degradation. Among these interferences, the inhibition effect of NO_3^- could be attributed to its quenching effect on hydroxyl radicals ($\cdot OH$) [65]. It is known that the 1O_2 -dominated degradation systems usually have good resistance to background interferences [66]. Hence, the relatively high 1O_2 yield in the $C_3N_{5-x}O$ piezocatalytic system should be a key factor for maintaining the TC degradation performance under high-salt conditions (Fig. S19). Interestingly, the presence of HCO_3^- has shown a positive effect on the degradation of TC, which could be attributed to its activation effect on H_2O_2 in ROS generation [67].

The HPLC-MS approach was used to identify the degradation intermediates of TC. As shown in Fig. S11, nine intermediates with mass peak located at 415 (P1), 417 (P2), 339 (P3), 274 (P4), 194 (P5), 461 (P6), 475 (P7), 290 (P8), and 274 (P9) are detected in the $C_3N_{5-x}O$ piezocatalytic system. Based on these intermediates, the possible degradation pathways are proposed in Fig. S12, where it can be seen that the primary pathways include deamination, dealkylation, terminal oxidation, and ring opening. The final step may involve the conversion of the ring-opening products to CO_2 , H_2O , and other low molecular products.

3.2.2. Piezocatalytic H_2O_2 production and piezocatalytic Fenton

Before establishing various piezocatalytic H_2O_2 production systems, a standard curve of H_2O_2 concentration-absorbance was initially developed (Fig. S13). Similar to its piezocatalytic degradation performances, $C_3N_{5-x}O$ also showed the highest H_2O_2 production with a rate of $0.615\ mM/g/h$ in the absence of any sacrificial agent, which was

much greater than that obtained from pristine C_3N_5 and single-defect C_3N_5 (Fig. 5a). Additionally, O sites outperform N vacancies in piezocatalytic H_2O_2 production, which is similar to piezocatalytic degradation experiments due to the superior O_2 activation ability of O sites. And defect engineering also improves the piezoelectric H_2O_2 production of C_3N_4 . The extremely low yields of H_2O_2 in the absence of catalysts highlight the crucial function of catalysts in piezocatalytic systems.

In general, the formation and decomposition of H_2O_2 may occur simultaneously in the reaction [2,68]. To further investigate the H_2O_2 production in the different piezocatalytic systems, their first-order and zero-order kinetic models were calculated to simulate the H_2O_2 decomposition constant (K_d) and formation constant (K_f) via Eq. (1). In Fig. 5b, the K_d and K_f for several piezocatalytic systems are summarized. Comparable K_d values were found for all C_3N_4 - and C_3N_5 -based catalysts, proving that defect engineering did not significantly speed up the decomposition of H_2O_2 . In comparison to other catalysts, $C_3N_{5-x}O$ has a much higher K_f value ($5.23\ \mu M/min$), demonstrating that dual-defect engineering is advantageous to the accumulation of H_2O_2 . The formation of H_2O_2 in the $C_3N_{5-x}O$ piezocatalytic system in the presence of TC is comparable to that in the absence of TC, which also indicates that the $C_3N_{5-x}O$ does not excessively decompose H_2O_2 (Fig. S14). The correlation between pH and H_2O_2 yield was examined, as seen in Fig. 5c. $C_3N_{5-x}O$ has a higher piezocatalytic H_2O_2 production under acidic circumstances (pH = 3) compared to neutral and alkaline conditions, reaching $0.703\ mM/g/h$. Because H_2O_2 synthesis is a proton-coupled electron transfer process, the H_2O_2 production is affected by pH [2].

$$[H_2O_2] = \frac{K_f}{K_d}(1 - e^{-K_d t}) \quad (1)$$

The mechanism of piezocatalytic H_2O_2 generation for different catalysts was further investigated using quenching experiments (Figs. 5d and S15). As a quencher for $O_2^{\cdot -}$ [2,32,69,70], p-benzoquinone (BQ) exhibited a high inhibitory effect (from $0.5129\ mM$ to $0.1582\ mM$), indicating that the formation of $O_2^{\cdot -}$ is a key step in the generation of H_2O_2 . In addition, the generation of H_2O_2 under an N_2 atmosphere is also severely inhibited from $0.5129\ mM$ to $0.1939\ mM$, which further indicates that the reduction of O_2 is the main path for the generation of H_2O_2 (Eqs. 2–5). The limited suppression of H_2O_2 production (from $0.5129\ mM$ to $0.3338\ mM$) by ethylenediaminetetraacetic acid disodium salt (EDTA2Na) as a quencher of hole (h^+) suggests that h^+ oxidation is not the primary step for H_2O_2 production (Eq. (6)) [2]. Isopropanol (IPA) acts as a $\cdot OH$ quencher to accelerate the generation of H_2O_2 from $0.5129\ mM$ to $0.5924\ mM$ [71], indicating that $\cdot OH$ is not the key step in the generation of H_2O_2 , and IPA acts as an electron sacrificial agent to accelerate the reaction. The trend of the quenching effect was consistent across all C_3N_5 -based catalysts, demonstrating that defect engineering did not alter the relative abundance of active species. Additionally, the effects of dose, ultrasonic power, and temperature on the piezocatalytic production of H_2O_2 were researched using $C_3N_{5-x}O$ as piezocatalyst (Fig. 5e). As the catalyst dosage increased from $0.125\ g/L$ to $1\ g/L$, the accumulation of H_2O_2 increased from $0.2718\ mM$ to $0.6268\ mM$ in 100 min. Consistent with the degradation experiments, a higher temperature is not conducive to H_2O_2 generation, which is attributed to the decrease of oxygen content and the self-decomposition of H_2O_2 at a higher temperature. Excitingly, in the absence of any sacrificial agent, the $C_3N_{5-x}O$ piezocatalytic system possesses a higher H_2O_2 production performance than many previous reports (Fig. 5f) [2,32,49,50,68,71–75].



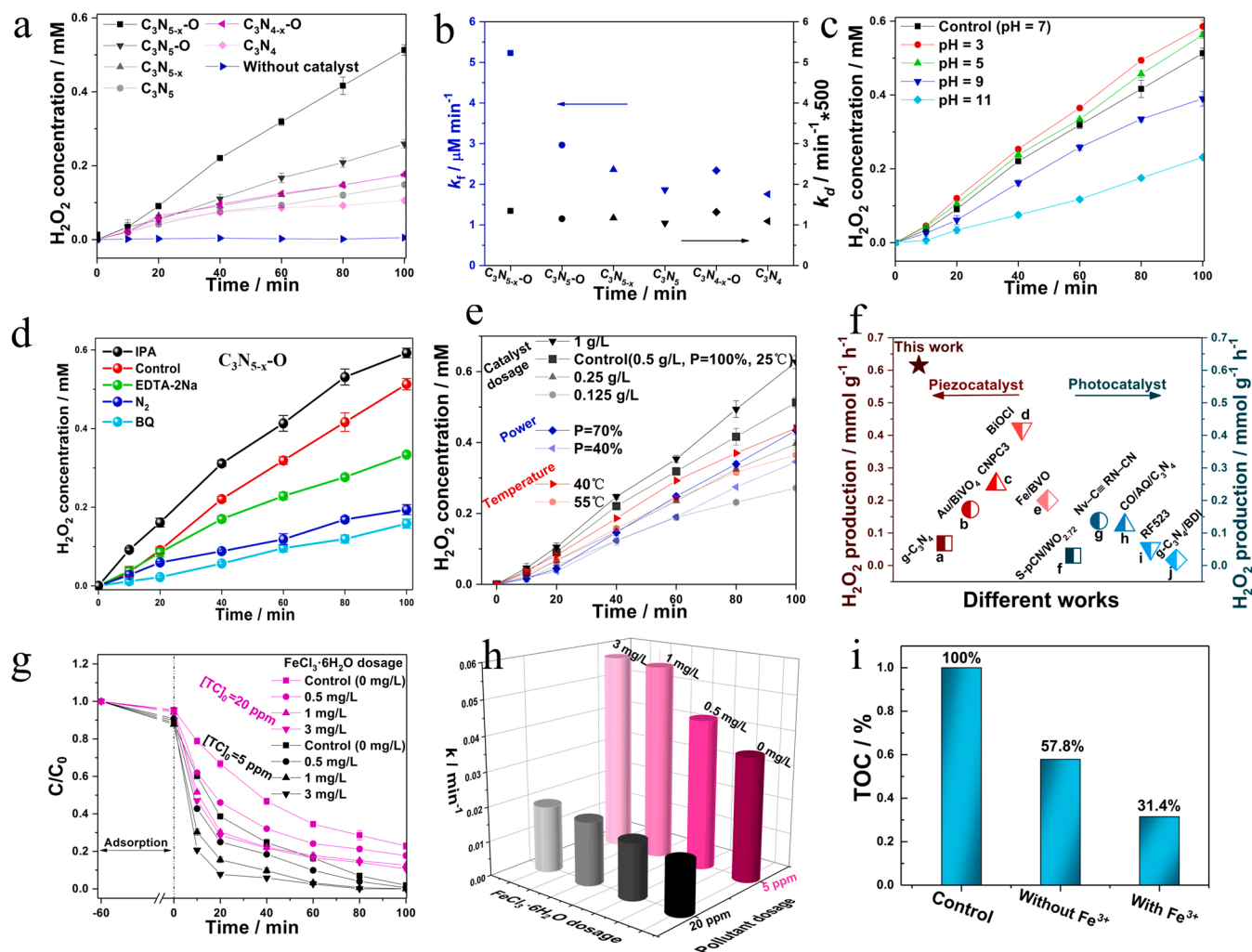


Fig. 5. Piezocatalytic H_2O_2 production and piezocatalytic Fenton performance. (a) Piezocatalytic H_2O_2 production of different catalysts, (b) the decomposition constant (K_d) and formation constant (K_f) of H_2O_2 . The influence of (c) solution pH, (d) different quenchers, and (e) different parameters, including dosage, power, and temperature on H_2O_2 production. (f) Comparison of H_2O_2 yield in this work with other literatures. (g) The effect of $\text{FeCl}_3 \cdot 6\text{H}_2\text{O}$ dose on piezocatalytic Fenton system and (h) the corresponding kinetic constants. (i) TOC removal rates of different systems.



Although the $\text{C}_3\text{N}_{5-x}\text{O}$ piezocatalytic system is effective at producing H_2O_2 , it is ineffective in activating it to remove pollutants (Fig. S16). Introducing Fe species to construct an in-situ Fenton system is a valuable strategy to enhance the piezocatalytic degradation properties of $\text{C}_3\text{N}_{5-x}\text{O}$. As shown in Fig. S17, Fe^{3+} has better catalytic performance than Fe^{2+} . This should be attributed to the fact that Fe^{3+} consumes piezoelectric electrons to promote the separation of piezoelectric electron/holes and improves the catalytic performance, which should be similar to the consumption of photogenerated electrons to promote electron/hole separation [76]. As the Fe source for an in-situ Fenton system, $\text{FeCl}_3 \cdot 6\text{H}_2\text{O}$ was chosen (Fig. 5 g, h). As in Eqs. 7–9, Fe^{3+} is first reduced to Fe^{2+} , which then undergoes a Fenton reaction with H_2O_2 . When the concentration of TC is 5 ppm, adding a small amount of $\text{FeCl}_3 \cdot 6\text{H}_2\text{O}$ (1 mg/L) can increase the degradation rate constant of TC to 0.0561 min^{-1} . The degradation rate constant of TC increased to 0.0571 min^{-1} when $\text{FeCl}_3 \cdot 6\text{H}_2\text{O}$ was raised to 3 mg/L, indicating that the improvement of TC degradation rate was limited by the abundance of H_2O_2 . When the TC concentration was raised to 20 ppm, a similar effect was seen, showing that 1 mg/L of $\text{FeCl}_3 \cdot 6\text{H}_2\text{O}$ was the right amount to add for in-situ Fenton. The in-situ Fenton system improved the TOC removal rate to 68.6% (Fig. 5i), which should be attributed to

the high concentration of $\bullet\text{OH}$ (Fig. S18).



3.3. Characterization of reactive species dominated by $\bullet\text{OH}$

To further understand the mechanism of different piezocatalytic degradation systems, quenching experiments and ESR trapping experiments were employed (Fig. 6). And the pseudo-first-order kinetic fitting on quenching experiments were summarized in the supporting information (Fig. S21). The strongest inhibitory impact in the $\text{C}_3\text{N}_{5-x}\text{O}$ piezocatalytic system is possessed by IPA (from 0.0965 min^{-1} to 0.0014 min^{-1}), highlighting the critical role of $\bullet\text{OH}$. Furthermore, furfuryl alcohol (FFA) and BQ also exhibited strong inhibitory effects on the $\text{C}_3\text{N}_{5-x}\text{O}$ piezocatalytic system, indicating that $^1\text{O}_2$ and O_2^- are also important ROS. Under a nitrogen atmosphere, the removal of TC was inhibited, further indicating that activation of oxygen to generate ROS is a key step (Fig. S22). Since EDTA2Na showed only moderate inhibition (0.0685 min^{-1}), it may be concluded that h^+ had the least important

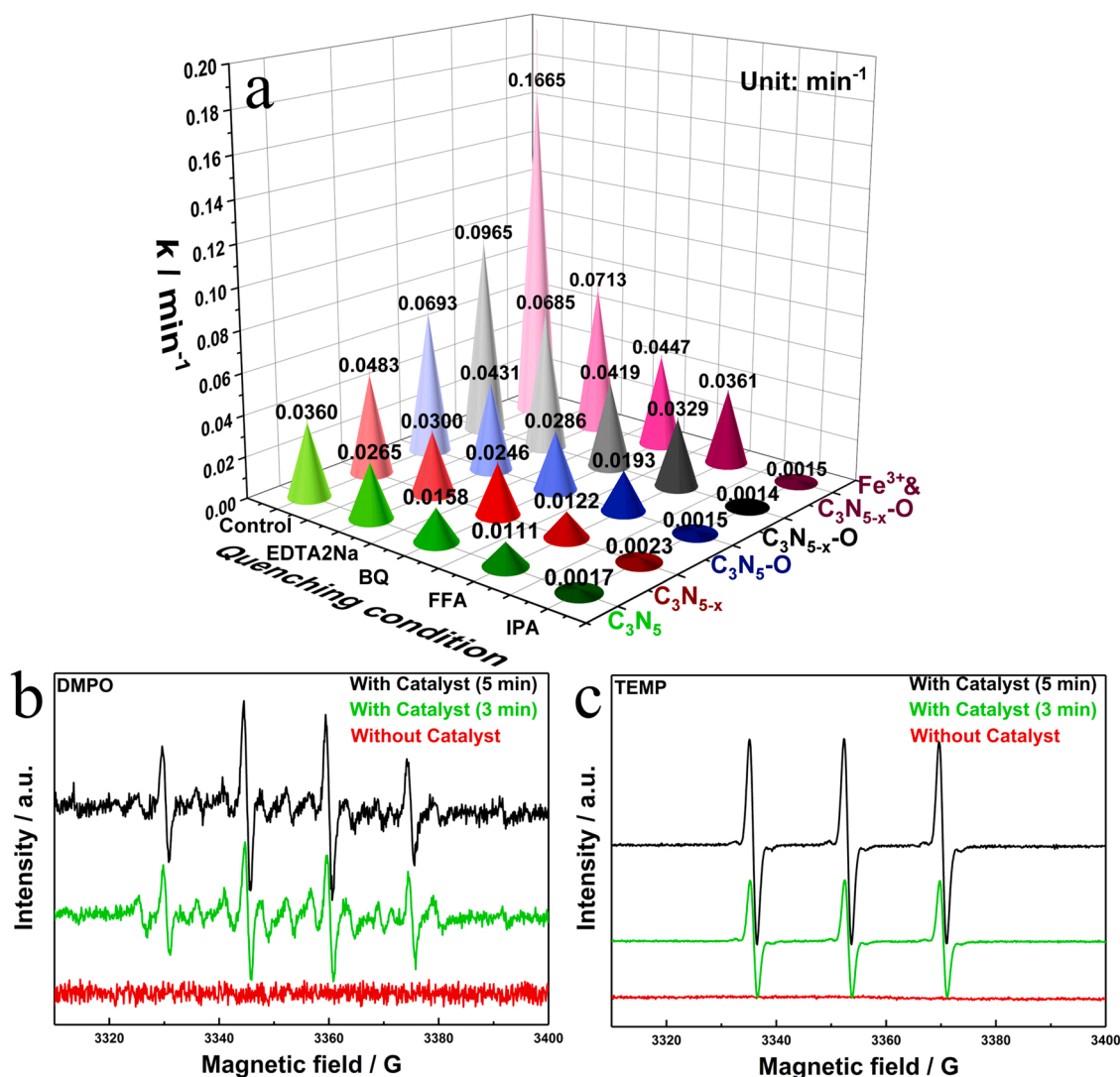
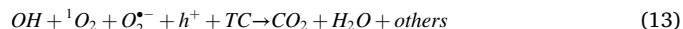


Fig. 6. The corresponding kinetic constants of quenching experiments in different piezocatalytic degradation systems (a). The ESR signal of (b)·OH and (c) 1O_2 in C_3N_{5-x} -O piezocatalytic system.

role in the degradation of TC. The fact that the quenching trends of both piezocatalytic degradation systems and the piezocatalytic Fenton system were identical showed that neither defect engineering nor the addition of Fe species would alter the relative contribution of active species. This is also similar to the H_2O_2 generation experiment. Additionally, utilizing DMPO and TEMP as traps, the existence of the two most significant ROS ($\cdot OH$ and 1O_2) in the C_3N_{5-x} -O piezocatalytic system was further determined. And the piezocatalytic degradation can be summarized in Eqs. (2)–(6) and (10)–(13).

Although defect engineering or the introduction of iron species did not change the relative contribution of various active species ($\cdot OH > ^1O_2 > O_2^- > h^+$), it did change the absolute abundance of active species. The increased TOC removal rate in the C_3N_{5-x} -O piezocatalytic Fenton system should be attributed to the production of high-yield·OH. According to Fig. S18, the piezocatalytic Fenton system produces 2.67 times more·OH than that of the conventional piezocatalytic system. After dual-defect engineering, the abundance of·OH, 1O_2 , and O_2^- was also significantly higher than that of single-defect C_3N_5 and pristine C_3N_5 , indicating that the defect engineering simultaneously enhanced the production of ROS (Figs. S18–S20).



3.4. PFM response and theoretical study further understands the piezoelectric nature and subsequent chemical processes on the surface of C_3N_{5-x} -O

PFM was used to test the piezoelectric response of the as-prepared C_3N_{5-x} -O to confirm its piezoelectric nature. The distinct polarization direction (Fig. 7a) and polarization degree (Fig. 7b) shown by the variation in amplitude and phase in various areas verifies the piezoelectric characteristics of C_3N_{5-x} -O [49,77,78]. A bias voltage was used to investigate the piezoelectric response of local locations. As illustrated in Fig. 7c, a well-characterized $\sim 160^\circ$ piezoelectric response phase reversal hysteresis loop and a conventional piezoelectric butterfly ring were achieved. Compared to C_3N_5 , the as-prepared C_3N_{5-x} -O has a larger maximum amplitude and piezoelectric response (Fig. S2b).

C_3N_{5-x} -O has a bigger specific surface area and a lower thickness than C_3N_5 , which should be one of the reasons for its higher

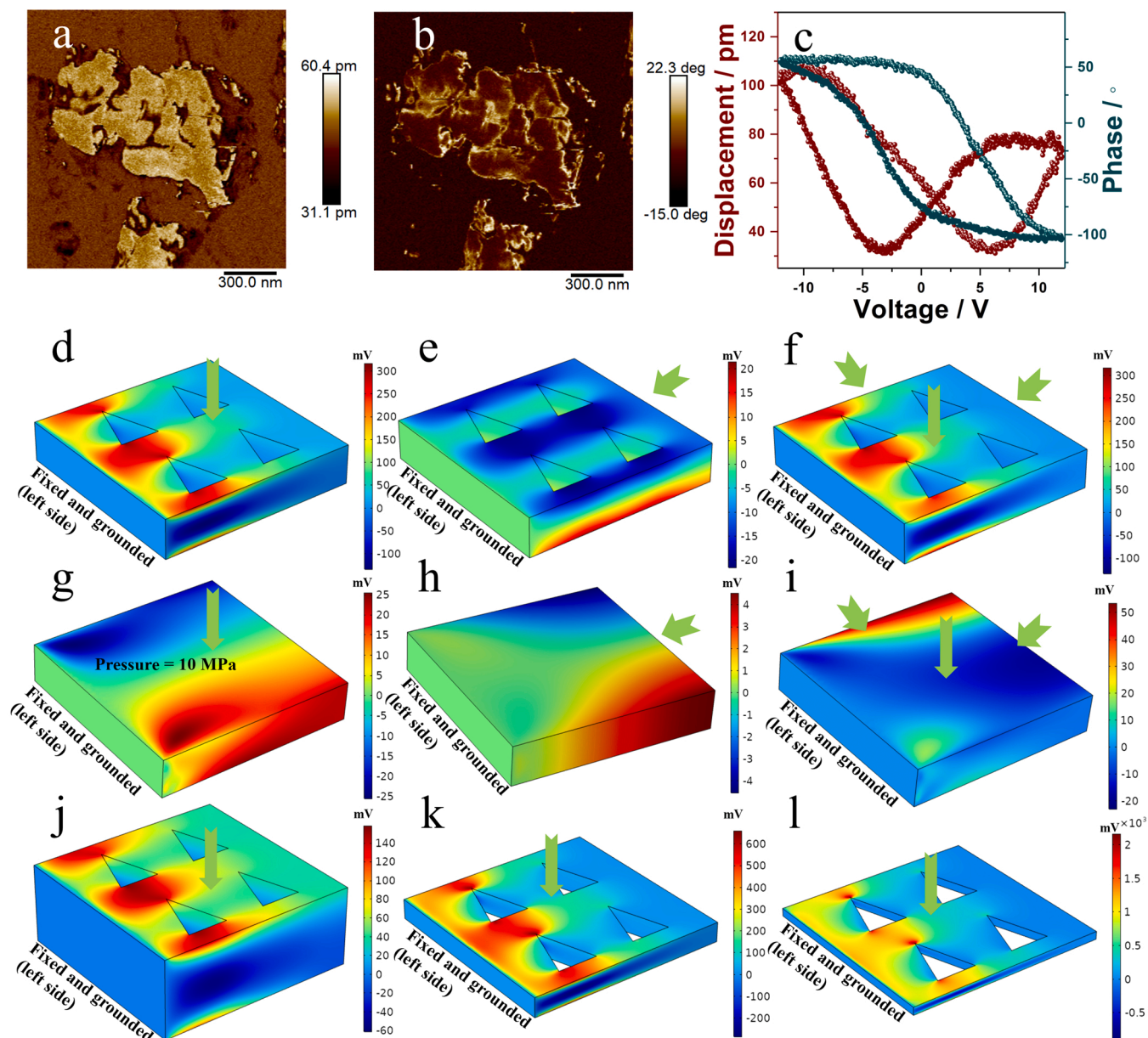


Fig. 7. (a) PFM amplitude image, (b) phase image, (c) the phase hysteresis loop and amplitude butterfly loop of $C_3N_{5-x}O$. The piezoelectric potential distribution calculated by FEM: (d, e, and f) porous nanosheet models, (g, h, and i) smooth nanosheet models, (j, k, and l) porous nanosheet models with different thickness (20 nm, 5 nm, and 2 nm, respectively).

piezocatalytic activity (Figs. 1d, S2, and S23). To further understand the enhanced phenomenon, COMSOL Multiphysics was used to simulate the piezoelectric effect. We set the boundary load to 10 MPa because the bubbles collapse during sonication and produce a high pressure of about 10 MPa on the catalyst [2]. And the arrow points in the direction of a pressure of 10 MPa. First, porous and smooth nanosheet models were built to approximate the porous $C_3N_{5-x}O$ nanosheet (Fig. 7d-f) and the C_3N_5 nanosheet (Fig. 7g-i). It is important to note that the piezopotential difference in porous models is always higher than that in smooth models, regardless of where the pressure originates from, revealing the promoted energy harvest and conversion ability of $C_3N_{5-x}O$. In $C_3N_{5-x}O$, more triangular pores made by triazine and triazole units may be exposed due to the increased specific surface area. Then, the effect of thickness on piezoelectricity was simulated. As shown in Fig. 7j-l, when the thickness is decreased from 20 nm to 2 nm, the potential difference is largely enhanced, also illustrating that the $C_3N_{5-x}O$ thin-layer nanosheet possesses enhanced energy harvest and conversion ability.

Although piezopotential appears to be a useful activity descriptor for piezocatalysis, comprehending piezocatalysis requires more than a physical understanding of catalysts [5]. The chemical processes on the catalyst surface, such as the adsorption behavior of reactive substrates, the charge transfer behavior after adsorption, and the reaction pathway in the catalytic process, are also important factors restricting the overall performance of a piezocatalyst. A series of DFT calculations were performed to understand the chemical processes deeply. The models of pristine C_3N_5 , single-defect C_3N_5 , and dual-defect C_3N_5 were built as shown in Fig. 8a-d. The adsorption of the substrate on the catalyst surface is a prerequisite for the catalytic reaction to proceed. All the adsorption data are summarized in Fig. 8e (adsorption energies of TC), Fig. S24 (adsorption configuration of TC), Fig. 8f (adsorption energies of O_2), and Fig. S25 (adsorption configuration of O_2). In single-defect C_3N_5 -based materials, N vacancies favor TC adsorption (adsorption energy, -0.639 eV), while O doping promotes O_2 adsorption (adsorption energy, -0.144 eV). The oxygen temperature programming desorption

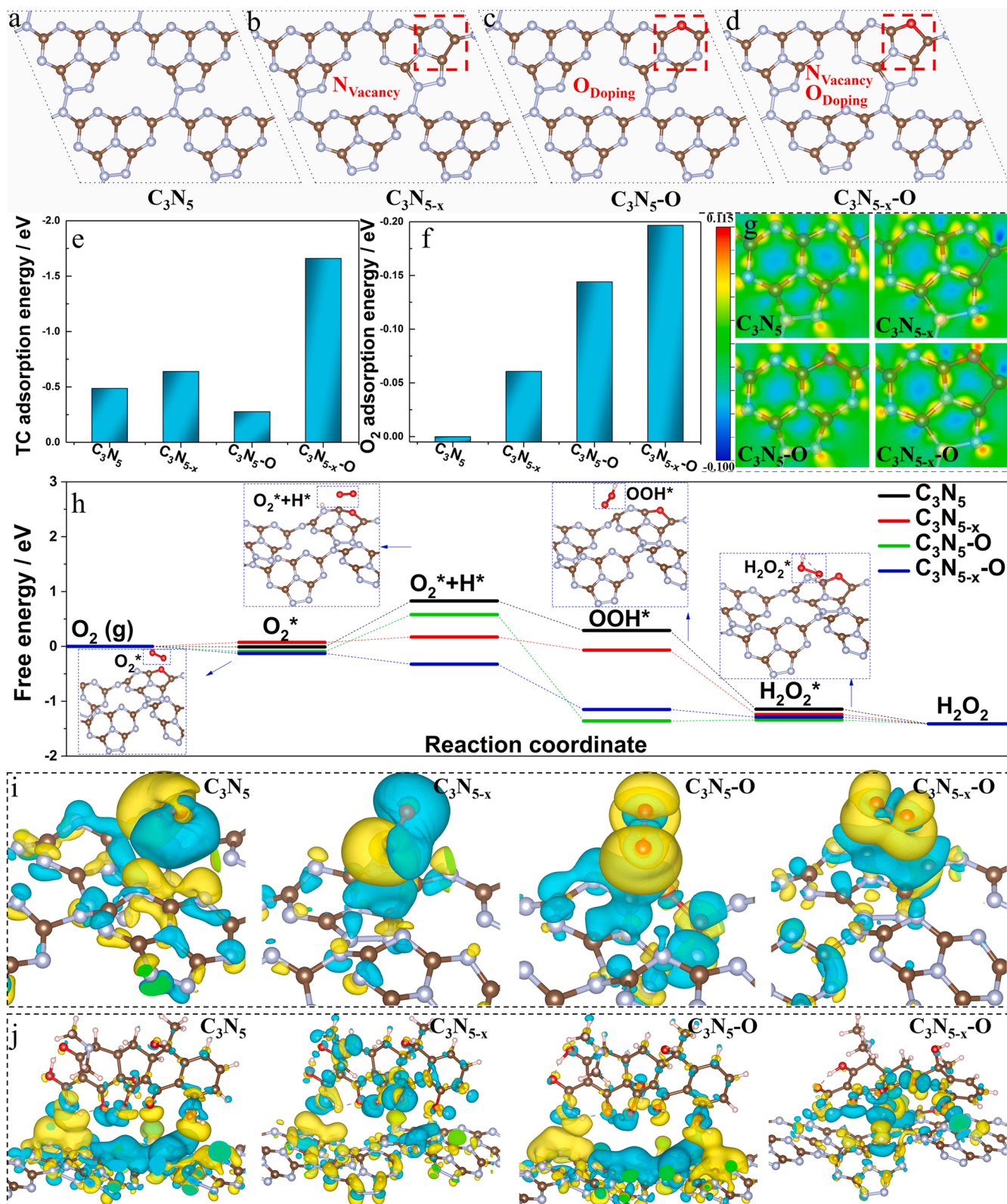


Fig. 8. The structure models of (a) C_3N_5 , (b) C_3N_{5-x} , (c) C_3N_5-O , and (d) $C_3N_{5-x}-O$. (e) TC adsorption energy and (f) O_2 adsorption energy on different C_3N_5 -based catalysts. (g) The two-dimensional charge density difference of different C_3N_5 -based catalysts. (h) Free energy data of different piezocatalytic H_2O_2 production systems. The charge density difference data of (i) O_2 /catalysts and (j) TC/catalysts. Yellow and blue represent electron accumulation and dissipation, respectively.

(O₂-TPD) shows that C₃N_{5-x}-O has a stronger O₂ adsorption capacity than others, which strongly supports our calculation conclusions (Fig. S26 a). In addition, TC adsorption experiments also confirmed that materials with N vacancies were more favorable for TC adsorption (Fig. S26 b). Furthermore, the dual-defect C₃N₅ had high TC (adsorption energy, -1.660 eV) and O₂ (adsorption energy, -0.197 eV) adsorption capabilities at the same time. It is worth noting that the bond length of O₂ is longer when adsorbed on defect C₃N₅ (Table S4), suggesting that defect engineering can further activate O₂ [32] which was advantageous for subsequent TC degradation and H₂O₂ production. The charge density difference results, as shown in Figs. 8i and 8j, reveal electron transfer following O₂ or TC adsorption. Similar to the adsorption energy data, the charge redistribution in the C₃N_{5-x}/TC model is much more impressive than in the model of C₃N₅-O/TC, demonstrating the stronger interaction between C₃N_{5-x} and TC. Similar phenomena also occur between C₃N₅-O and O₂, indicating that O doping is beneficial for the adsorption and activation of O₂. Furthermore, dual-defect C₃N₅ showed considerably improved charge transfer from C₃N_{5-x}-O to O₂ and charge transfer from TC to C₃N_{5-x}-O, signaling that dual-defects exhibit a synergistic effect and contribute to the enhanced piezocatalytic activity. The charge state on the surfaces of various catalysts was explored further (Fig. 8g), and it was discovered that defect engineering aids in the unequal redistribution of surface charges, which supports increasing polarization and raising the piezopotential. This is also consistent with the experimental fact that dual-defect C₃N₅ possesses the highest piezocatalytic performance. In addition, the Gibbs free energies of the two-electron oxidation reduction reaction (2e-ORR) with different C₃N₅-based catalysts were calculated (Fig. 8h). The H₂O₂ formation path of the catalyst after dual-defect engineering is smoother than other samples, indicating better H₂O₂ generation potential. Previous studies have shown that the production of OOH* is crucial to the activity of a 2e-ORR.[32,79,80] Obviously, the production of OOH* and consequent hydrogenation is more advantageous due to dual-defect engineering optimizing the reaction of [O₂* + H*] in the previous step.

The piezocatalytic mechanism of C₃N_{5-x}-O is summarized in Fig. 9. On the one hand, in the presence of pollutants, the piezoelectric effect can promote the separation of electron and hole, which are then transported to the active site. The O sites can effectively adsorb and activate O₂, which can be further converted into ROS (path 1) or H₂O₂ (path 2). The N vacancies can promote the adsorption of TC molecules and enrich the pollutants near the catalyst to wait for the attack of ROS. And the dual-defect engineering has a synergistic effect, which can efficiently

adsorb/activate O₂ and adsorb TC at the same time. After the introduction of Fe species (path 3), the constructed in-situ Fenton system will generate a large number of ·OH, which further improves the mineralization efficiency of TC. On the other hand, in the absence of pollutants and Fe species (path 2), the constructed dual-defective C₃N₅ is an efficient catalyst for H₂O₂ production. The dual-defect site further optimizes not only the adsorption and activation of O₂ but also the generation of [OOH*] and the subsequent hydrogenation. In addition, efficient 2e-ORR [O₂ + 2 H⁺ + 2e⁻ → H₂O₂] rather than hole oxidation [2 H₂O + 2 h⁺ → H₂O₂ + 2 H⁺] is the principal pathway for H₂O₂ production. The dual-defect strategy improves the piezoelectric nature of C₃N₅, further optimizes the surface chemical process, and provides insights into the development of multifunctional piezocatalyst. So the C₃N_{5-x}-O has a better piezocatalytic performance than the conventional piezoelectric catalysts (Fig. S27).

To investigate whether O doping and N vacancy on other nitrogen-rich carbon nitrides are also beneficial for the enhancement of the piezocatalytic properties, theoretical simulations on C₃N₆, dual-defect C₃N₆ (denoted as C₃N_{6-x}-O), C₃N₇, and dual-defect C₃N₇ (C₃N_{7-x}-O) were conducted and the results are summarized in Fig. 10. As shown in Fig. 10 a, defect engineering increases the asymmetry of the molecular structure of the catalyst, leading to the enhancement in the polarization and piezoelectric properties. Defect engineering also causes the enriched charges near the O sites, the increased electron donation capability should be accountable for the effective activation of O₂. As descriptors of O₂ activation [32], adsorption energy data, O-O bond length, and charge transfer data also support this view (Fig. 10, b, c, and d). Therefore, it is considered that the construction of dual-defect sites including O doping and N vacancy should be a general strategy to enhance the piezocatalytic performance of other nitrogen-rich carbon nitrides.

3.5. The stability of different piezocatalytic systems

A crucial metric for assessing catalyst efficacy is stability. The stability of piezocatalytic H₂O₂ production, piezocatalytic degradation, and piezocatalytic Fenton were evaluated in detail. As shown in Fig. 11a, H₂O₂ rapidly accumulated to a high level within 3 h, and the growth rate slowed down within 3–9 h. The catalyst was still able to provide more than 95% of the initial H₂O₂ yield after 5 cycles (Fig. 11d), demonstrating its stability. When the solvent was replaced with tap water and Lihu water (Fig. 11b), the degradation trend of pollutants was consistent with that when ultrapure water was used as the solvent. In actual

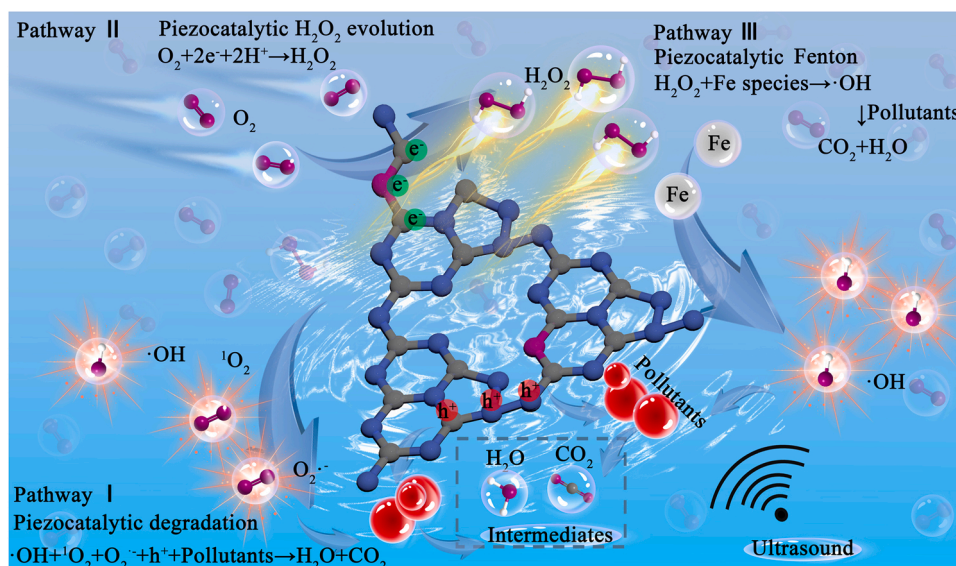


Fig. 9. Schematic diagram of different C₃N_{5-x}-O piezocatalytic systems.

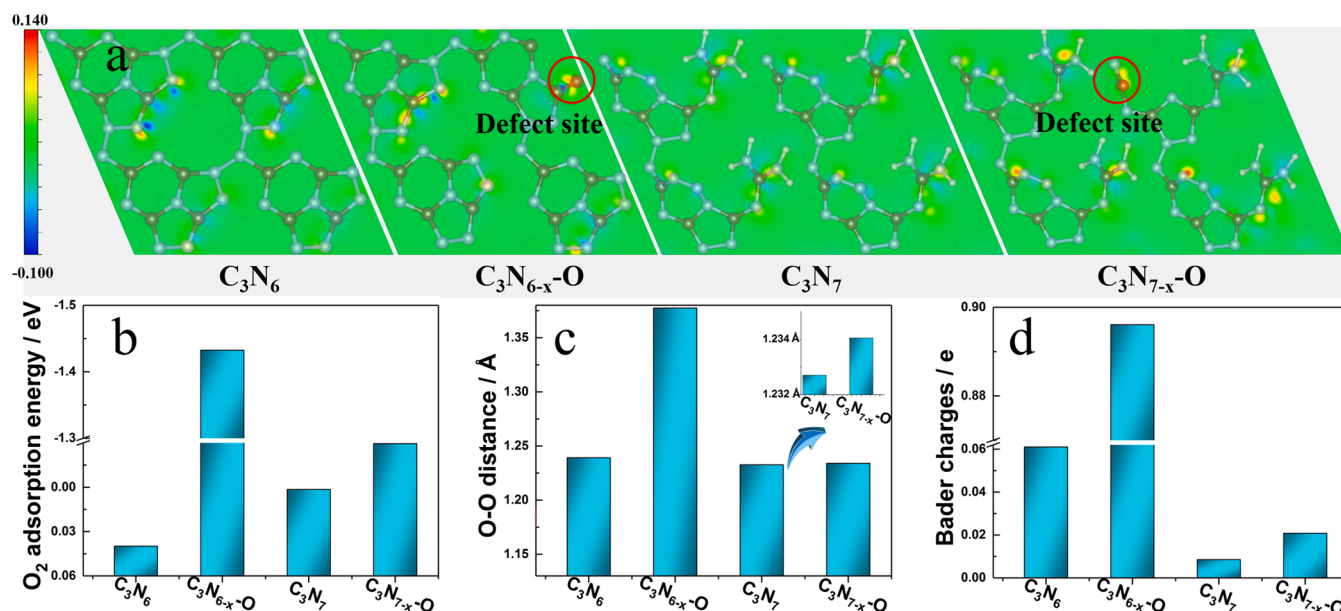


Fig. 10. (a) The structure models and two-dimensional charge density difference, (b) O_2 adsorption energy, (c) O-O distance, and (d) bader charges of nitrogen-rich carbon nitrides.

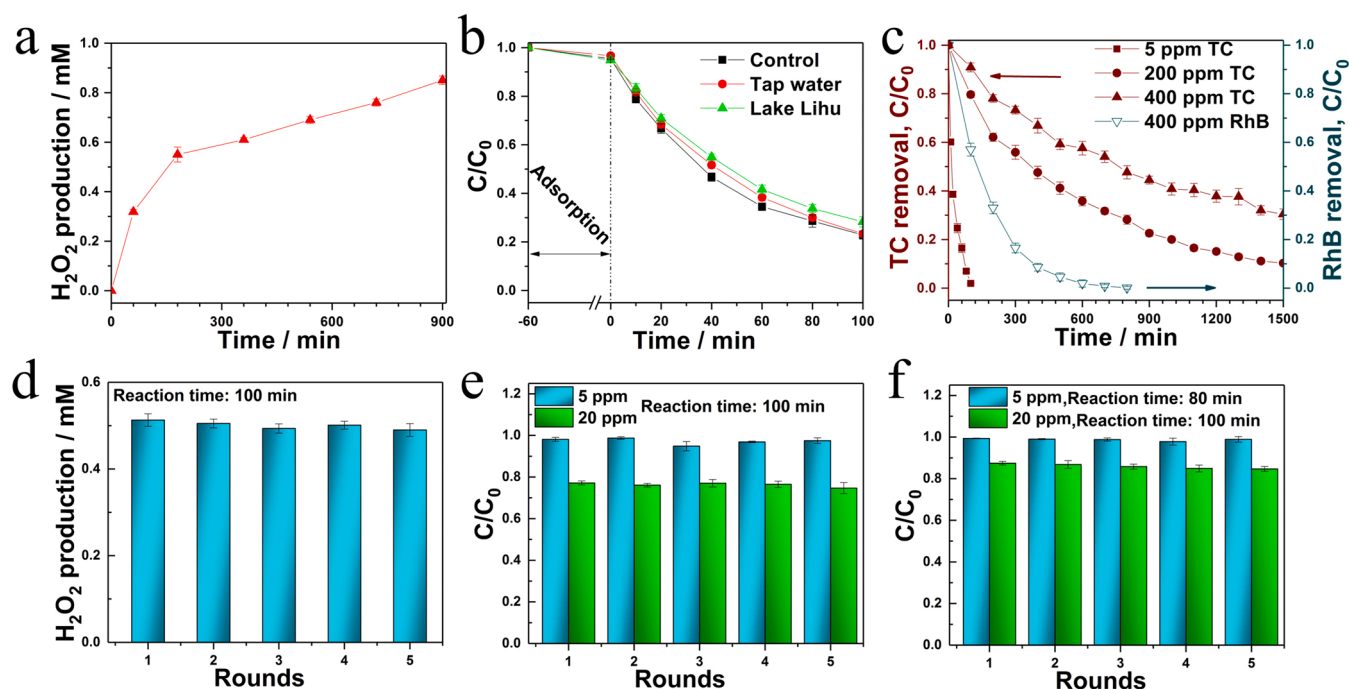


Fig. 11. The stability of $C_3N_{5-x}O$ piezocatalytic systems. (a) H_2O_2 accumulation curve. (b) TC degradation curves under different water. (c) Degradation curves of TC and RhB at high concentrations. Cycling performance of $C_3N_{5-x}O$ (d) piezocatalytic H_2O_2 production, (e) piezocatalytic degradation, and (f) piezocatalytic Fenton.

conditions, high-concentration wastewater is usually present. Examples include effluent from pig farms, electroplating, ink manufacturing, printing, and dyeing. To verify that the piezocatalytic system can handle high-concentration pollutants, we used high-concentration TC and RhB as substrates to investigate the removal effect. A high removal efficiency can be achieved simply by prolonging the reaction time without increasing the catalyst concentration. Moreover, compared with repeating the degradation of low-concentration pollutants many times, processing concentrated pollutants is more time-saving and cost-effective. As shown in Fig. 11e f, both piezocatalytic degradation and

piezocatalytic Fenton exhibited greater than 95% stability within 5 cycles. In addition, the morphology and crystal structure of $C_3N_{5-x}O$ after use are almost unchanged, which also shows the stability of the catalyst and the potential for practical application (Fig. S28).

4. Conclusions

2D-layered C_3N_5 containing O sites and N vacancies were synthesized by a simple thermal polymerization and thermal etching strategy. The $C_3N_{5-x}O$ was applied to piezocatalytic degradation, H_2O_2

production, and Fenton to further understand and verify its piezocatalytic performance. Under optimized conditions, C_3N_5-xO can achieve complete and rapid piezocatalytic degradation of TC and RhB. And the piezocatalytic Fenton system strengthens this effect. Because defect engineering increases the formation of $\cdot OH$, 1O_2 , and $O_2^{\cdot -}$ rather than altering the degradation pathway, the piezocatalytic degradation system could still function well in the presence of high salt or high concentrations of contaminants. The C_3N_5-xO piezoelectric system effectively produces H_2O_2 with a yield of 0.615 mM/g/h in the absence of sacrificial agents. FEM calculations and DFT simulations further confirm the origin of C_3N_5-xO piezocatalysis. The 2D defect structure enhances the in-plane polarization, exposes more active sites, optimizes the electronic structure, and creates an active surface for the subsequent chemical process. Additionally, the O sites are better suited for the adsorption and activation of O_2 , the N vacancies are ideally placed for the adsorption of TC, and the dual-defect sites have a synergistic effect to exhibit faster pollutant removal ability and H_2O_2 generation ability. In different piezoelectric catalytic processes, the contribution of active species was further analyzed, and the potential TC degradation pathways and H_2O_2 generation pathways were proposed. The results presented in this work deepened our understanding on the relative activity and synergistic effect of the defect sites, which would be useful for the rational design of carbon nitride catalysts for environmental remediation and the generation of high-value chemicals.

CRediT authorship contribution statement

Cheng Fu: Investigation, Methodology, Software, Visualization, Data curation, Writing – original draft, Writing – review & editing. **Tao Wu:** Software, Data curation. **Guowei Sun:** Software, Writing – review & editing. **Guofeng Yin:** Supervision. **Chan Wang:** Supervision, Funding acquisition. **Guoxia Ran:** Supervision, Writing – review & editing. **Qijun Song:** Investigation, Funding acquisition, Writing – review & editing.

Declaration of Competing Interest

The authors declare that they have no known competing financial interests or personal relationships that could have appeared to influence the work reported in this paper.

Data availability

Data will be made available on request.

Acknowledgments

This work is supported by the Natural National Science Foundation of China (51973083), National First-Class Discipline Program of Food Science and Technology (JUFSTR20180301), and Fundamental Research Funds for the Central Universities (JUSRP22027). We would like to acknowledge the work of Central Laboratory, School of Chemical and Material Engineering, Jiangnan University.

Appendix A. Supporting information

Supplementary data associated with this article can be found in the online version at [doi:10.1016/j.apcatb.2022.122196](https://doi.org/10.1016/j.apcatb.2022.122196).

References

- [1] Y. Wang, Y. Xu, S. Dong, P. Wang, W. Chen, Z. Lu, D. Ye, B. Pan, D. Wu, C. D. Vecitis, G. Gao, Ultrasonic activation of inert poly(tetrafluoroethylene) enables piezocatalytic generation of reactive oxygen species, *Nat. Commun.* 12 (2021) 3508.
- [2] R. Tang, D. Gong, Y. Zhou, Y. Deng, C. Feng, S. Xiong, Y. Huang, G. Peng, L. Li, Z. Zhou, Unique $g-C_3N_4$ /PDI- $g-C_3N_4$ homojunction with synergistic piezo-

- photocatalytic effect for aquatic contaminant control and H_2O_2 generation under visible light, *Appl. Catal. B, Environ.* 303 (2022), 120929.
- [3] F. Gao, M. Fang, S. Zhang, M. Ni, Y. Cai, Y. Zhang, X. Tan, M. Kong, W. Xu, X. Wang, Symmetry-breaking induced piezocatalysis of Bi_2S_3 nanorods and boosted by alternating magnetic field, *Appl. Catal. B, Environ.* 316 (2022), 121664.
- [4] C. Su, R. Li, C. Li, W. Wang, Piezo-promoted regeneration of Fe^{2+} boosts peroxydisulfate activation by $Bi_2Fe_4O_9$ nanosheets, *Appl. Catal. B, Environ.* 310 (2022), 121330.
- [5] K. Wang, C. Han, J. Li, J. Qiu, J. Sunarso, S. Liu, The mechanism of piezocatalysis: energy band theory or screening charge effect? *Angew. Chem. Int. Ed.* 61 (2022), e202110429.
- [6] W.T. Ye Miao, Jun Han, Najun Li, Dongyun Chen, Qingfeng Xu, Jianmei Lu, Oxygen vacancy-induced hydroxyl dipole reorientation in hydroxyapatite for enhanced piezocatalytic activity, *Nano Energy* 100 (2022), 107473.
- [7] Q. Liu, D. Zhai, Z. Xiao, C. Tang, Q. Sun, C.R. Bowen, H. Luo, D. Zhang, Piezo-photoelectronic coupling effect of $BaTiO_3@TiO_2$ nanowires for highly concentrated dye degradation, *Nano Energy* 92 (2022), 106702.
- [8] X. Zhou, B. Shen, J. Zhai, N. Hedin, Reactive Oxygenated Species Generated on Iodide-Doped $BiVO_4/BaTiO_3$ Heterostructures with Ag/Cu Nanoparticles by Coupled Piezophototronic Effect and Plasmonic Excitation, *Adv. Funct. Mater.* 31 (2021), 2009594.
- [9] P. Wang, X. Li, S. Fan, X. Chen, M. Qin, D. Long, M.O. Tadé, S. Liu, Impact of oxygen vacancy occupancy on piezo-catalytic activity of $BaTiO_3$ nanobelt, *Appl. Catal. B, Environ.* 279 (2020), 119340.
- [10] S. Lan, C. Yu, F. Sun, Y. Chen, D. Chen, W. Mai, M. Zhu, Tuning piezoelectric driven photocatalysis by La-doped magnetic $BiFeO_3$ -based multiferroics for water purification, *Nano Energy* 93 (2022), 106792.
- [11] J.M. Wu, Y.-R. Chen, W.T. Kao, Ultrafine ZnO nanoparticles/nanowires synthesized on a flexible and transparent substrate: formation, water molecules, and surface defect effects, *ACS Appl. Mater. Inter.* 6 (2014) 487–494.
- [12] C. Wang, F. Chen, C. Hu, T. Ma, Y. Zhang, H. Huang, Efficient piezocatalytic H_2O_2 production of atomic-level thickness $Bi_4Ti_3O_{12}$ nanosheets with surface oxygen vacancy, *Chem. Eng. J.* 431 (2022), 133930.
- [13] C. Tan, X. Cao, X.-J. Wu, Q. He, J. Yang, X. Zhang, J. Chen, W. Zhao, S. Han, G.-H. Nam, M. Sindoro, H. Zhang, Recent advances in ultrathin two-dimensional nanomaterials, *Chem. Rev.* 117 (2017) 6225–6331.
- [14] J. Tan, S. Li, B. Liu, H.-M. Cheng, Structure, Preparation, and Applications of 2D Material-Based Metal–Semiconductor Heterostructures, *Small Struct.* 2 (2021), 2000093.
- [15] C. Hu, F. Chen, Y. Wang, N. Tian, T. Ma, Y. Zhang, H. Huang, Exceptional cocatalyst-free photo-enhanced piezocatalytic hydrogen evolution of carbon nitride nanosheets from strong in-plane polarization, *Adv. Mater.* 33 (2021), 2101751.
- [16] W. Feng, J. Yuan, L. Zhang, W. Hu, Z. Wu, X. Wang, X. Huang, P. Liu, S. Zhang, Atomically thin ZnS nanosheets: Facile synthesis and superior piezocatalytic H_2 production from pure H_2O , *Appl. Catal. B, Environ.* 277 (2020), 119250.
- [17] Y. Su, L. Zhang, W. Wang, X. Li, Y. Zhang, D. Shao, Enhanced H_2 evolution based on ultrasound-assisted piezo-catalysis of modified MoS_2 , *J. Mater. Chem. A* 6 (2018) 11909–11915.
- [18] W. Feng, J. Yuan, F. Gao, B. Weng, W. Hu, Y. Lei, X. Huang, L. Yang, J. Shen, D. Xu, X. Zhang, P. Liu, S. Zhang, Piezopotential-driven simulated electrocatalytic nanosystem of ultrasmall MoC quantum dots encapsulated in ultrathin N-doped graphene vesicles for superhigh H_2 production from pure water, *Nano Energy* 75 (2020), 104990.
- [19] H. Lei, M. Wu, F. Mo, S. Ji, X. Dong, Y. Jia, F. Wang, Z. Wu, Efficiently harvesting the ultrasonic vibration energy of two-dimensional graphitic carbon nitride for piezocatalytic degradation of dichlorophenols, *Environ. Sci. Nano* 8 (2021) 1398–1407.
- [20] H. Zhou, M. Wang, F. Wang, Oxygen-controlled photo-reforming of biopolymers to CO over Z-scheme $CdS@g-C_3N_4$, *Chem* 8 (2022) 465–479.
- [21] J. Luo, Y. Liu, C. Fan, L. Tang, S. Yang, M. Liu, M. Wang, C. Feng, X. Ouyang, L. Wang, L. Xu, J. Wang, M. Yan, Direct Attack and Indirect Transfer Mechanisms Dominated by Reactive Oxygen Species for Photocatalytic H_2O_2 Production on $g-C_3N_4$ Possessing Nitrogen Vacancies, *ACS Catal.* 11 (2021) 11440–11450.
- [22] S. Kumar Kuila, P. Kumbhakar, C. Sekhar Tiwary, T. Kumar, Kundu, Photon and vibration synergism on planar defects induced 2D-graphitic carbon nitride for ultrafast remediation of dyes and antibiotic ampicillin, *J. Mater. Sci.* 57 (2022) 8658–8675.
- [23] M. Zelisko, Y. Hanlunyuang, S. Yang, Y. Liu, C. Lei, J. Li, P.M. Ajayan, P. Sharma, Anomalous piezoelectricity in two-dimensional graphene nitride nanosheets, *Nat. Commun.* 5 (2014) 4284.
- [24] R.-C. Wang, Y.-C. Lin, H.-C. Chen, W.-Y. Lin, Energy harvesting from $g-C_3N_4$ piezoelectric nanogenerators, *Nano Energy* 83 (2021), 105743.
- [25] S.K. In Young Kim+, Xiaoyan Jin, Selvarajan Premkumar, Goutam Chandra, G.P. M. Nam-Suk Lee, Seong-Ju Hwang, Siva Umaphathy, Ajayan Vinu*, Ordered Mesoporous C_3N_5 with a Combined Triazole and Triazine Framework and Its Graphene Hybrids for the Oxygen Reduction Reaction (ORR), *Angew. Chem. Int. Ed.* 57 (2018) 17135–17140.
- [26] G.P. Mane, S.N. Talapaneni, K.S. Lakhi, H. Ilbeygi, U. Ravon, K. Al-Bahily, T. Mori, D.H. Park, A. Vinu, Highly Ordered Nitrogen-Rich Mesoporous Carbon Nitrides and Their Superior Performance for Sensing and Photocatalytic Hydrogen Generation, *Angew. Chem. Int. Ed.* 56 (2017) 8481–8485.
- [27] S. Qi, Y. Fan, J. Wang, X. Song, W. Li, M. Zhao, Metal-free highly efficient photocatalysts for overall water splitting: C_3N_5 multilayers, *Nanoscale* 12 (2020) 306–315.

- [28] J. Zhang, B. Jing, Z. Tang, Z. Ao, D. Xia, M. Zhu, S. Wang, Experimental and DFT insights into the visible-light driving metal-free C_3N_5 activated persulfate system for efficient water purification, *Appl. Catal. B, Environ.* 289 (2021).
- [29] I.Y. Kim, S. Kim, S. Premkumar, J.-H. Yang, S. Umaphathy, A. Vinu, Thermodynamically Stable Mesoporous C_3N_7 and C_3N_6 with Ordered Structure and Their Excellent Performance for Oxygen Reduction Reaction, *Small* 16 (2020), 1903572.
- [30] S.N. Talapaneni, G. Singh, I.Y. Kim, K. AlBahily, Aa.H. Al-Muhtaseb, A.S. Karakoti, E. Tavakkoli, A. Vinu, Nanostructured Carbon Nitrides for CO_2 Capture and Conversion, *Adv. Mater.* 32 (2020), 1904635.
- [31] S. Kim, G. Singh, C.I. Sathish, P. Panigrahi, R. Daiyan, X. Lu, Y. Sugi, I.Y. Kim, A. Vinu, Tailoring the Pore Size, Basicity, and Binding Energy of Mesoporous C_3N_5 for CO_2 Capture and Conversion, *Chem. – Asian J.* 16 (2021) 3999–4005.
- [32] P.M. Xu Zhang, Cong Wang, Liyong Gan, Xianjie Chen, Peng Zhang, Yang Wang, Hui Li, Lihua Wang, Kun Zheng, Unraveling the dual defect sites in graphite carbon nitride for ultra-high photocatalytic H_2O_2 evolution, *Energy Environ. Sci.* 15 (2022) 830–842.
- [33] B.X. Jing Zhang, Chao Shan, Weiming Zhang, Dionysios D. Dionysiou, Bingcai Pan, Roles of oxygen-containing functional groups of O-doped $g-C_3N_4$ in catalytic ozonation: Quantitative relationship and first-principles investigation, *Appl. Catal. B, Environ.* 292 (2021), 120155.
- [34] P.P.T.I.T. Okpalugo, H. Murphy, J. McLaughlin, N.M.D. Brown, High resolution XPS characterization of chemical functionalised MWCNTs and SWCNTs, *Carbon* 43 (2005) 153–161.
- [35] S.P. Dariya Dontsova, Marko Wehle, Zupeng Chen, Christian Fettkenhauer, Guylhaine Clavel, Markus Antonietti, Triazoles: A New Class of Precursors for the Synthesis of Negatively Charged Carbon Nitride Derivatives, *Chem. Mater.* 27 (2015) 5170–5179.
- [36] C. Yang, B. Wang, L. Zhang, L. Yin, X. Wang, Synthesis of layered carbonitrides from biotic molecules for photoredox transformations, *Angew. Chem. Int. Ed.* 56 (2017) 6627–6631.
- [37] H.Z. Weikang Wang, Shengbo Zhang, Yanyan Liu, Guozhong Wang, Chenghua Sun, Huijun Zhao, Potassium-ion-assisted regeneration of activecyano groups in carbon nitride nanoribbons: visible-light-driven photocatalytic nitrogen reduction, *Angew. Chem. Int. Ed.* 58 (2019) 16644–16650.
- [38] S.S. Sai Zhang, Pengcheng Gu, Ran Ma, Dongli Wei, Guixia Zhao, Tao Wen, Riffat Jehan, Baowei Hu, Xiangke Wang, Visible-light-driven activation of persulfate over cyano and hydroxyl group co-modified mesoporous $g-C_3N_4$ for boosting bisphenol A degradation, *J. Mater. Chem. A* 7 (2019) 5552.
- [39] Y.C. Piao Zhu, Jianlin Shi, Piezocatalytic Tumor Therapy by Ultrasound-Triggered and $BaTiO_3$ -Mediated Piezoelectricity, *Adv. Mater.* 32 (2020), 2001976.
- [40] W.E.C. Jyh Ming Wu, Yu. Ting Chang, Chih-Kai Chang, Piezo-Catalytic Effect on the Enhancement of the Ultra-High Degradation Activity in the Dark by Singleand Few-Layers MoS_2 Nanoflowers, *Adv. Mater.* 28 (2016) 3718–3725.
- [41] J. Dou, J. Cheng, Z. Lu, Z. Tian, J. Xu, Y. He, Biochar co-doped with nitrogen and boron switching the free radical based peroxodisulfate activation into the electron-transfer dominated nonradical process, *Appl. Catal. B, Environ.* 301 (2022), 120832.
- [42] Y.M. Li Li, Gaifang Chen, Jingsong Wang, Chunchang Wang, Oxygen-vacancy-enhanced piezo-photocatalytic performance of $AgNbO_3$, *Scr. Mater.* 206 (2022), 114234.
- [43] Y.W. Youyu Duan, Liyong Gan, Jiazhi Meng, Yajie Feng, Kaiwen Wang, Kai Zhou, Cong Wang, Xiaodong Han, Xiaoyuan Zhou, Amorphous Carbon Nitride with Three Coordinate Nitrogen (N_3C) Vacancies for Exceptional NO_x Abatement in Visible Light, *Adv. Energy Mater.* 11 (2021), 2004001.
- [44] W.B. Xiaogang Li, Lei Zhang, Shi Tao, Wangsheng Chu, Qun Zhang, Yi Luo, Changzheng Wu, Yi Xie, Single-Atom Pt as Co-Catalyst for Enhanced Photocatalytic H_2 Evolution, *Adv. Mater.* 28 (2016) 2427–2431.
- [45] G.L. Guigang Zhang, Zhi-An Lan, Lihua Lin, Aleksandr Savateev, Tobias Heil, Spiros Zafeirotas, Xinchun Wang, Markus Antonietti, Optimizing Optical Absorption, Exciton Dissociation, and Charge Transfer of a Polymeric Carbon Nitride with Ultrahigh Solar Hydrogen Production Activity, *Angew. Chem. Int. Ed.* 56 (2017) 13445–13449.
- [46] P.D. Yong Wang, Hongzhe Pan, Lin Fu, Yu Zhang, Jie Chen, Youwei Du, Nuijiang Tang, Gang Liu, Increasing Solar Absorption of Atomically Thin 2D Carbon Nitride Sheets for Enhanced Visible-Light Photocatalysis, *Adv. Mater.* 31 (2019), 1807540.
- [47] H.W. Yuanyi Zhou, Xuechen Liu, Simeng Qiao, Dengkui Shao, Jing Zhou, Ling Zhang, Wenzhong Wang, Direct piezocatalytic conversion of methane into alcohols over hydroxyapatite, *Nano Energy* 79 (2021), 105449.
- [48] Z. Chen, H. Zhou, F. Kong, M. Wang, Piezocatalytic oxidation of 5-hydroxymethylfurfural to 5-formyl-2-furancarboxylic acid over Pt decorated hydroxyapatite, *Appl. Catal. B, Environ.* 309 (2022).
- [49] Y. Wei, Y. Zhang, W. Geng, H. Su, M. Long, Efficient bifunctional piezocatalysis of $Au/BiVO_4$ for simultaneous removal of 4-chlorophenol and $Cr(VI)$ in water, *Appl. Catal. B, Environ.* 259 (2019), 118084.
- [50] Y. Wei, Y. Zhang, J. Miao, W. Geng, M. Long, In-situ utilization of piezo-generated hydrogen peroxide for efficient p-chlorophenol degradation by Fe loading bismuth vanadate, *Appl. Surf. Sci.* 543 (2021), 148791.
- [51] Q. Zhang, L. Jiang, J. Wang, Y. Zhu, Y. Pu, W. Dai, Photocatalytic degradation of tetracycline antibiotics using three-dimensional network structure perylene diimide supramolecular organic photocatalyst under visible-light irradiation, *Appl. Catal. B, Environ.* 277 (2020), 119122.
- [52] J. Wang, W. Shi, D. Liu, Z. Zhang, Y. Zhu, D. Wang, Supramolecular organic nanofibers with highly efficient and stable visible light photooxidation performance, *Appl. Catal. B, Environ.* 202 (2017) 289–297.
- [53] X. Liu, J. Lu, B.A. Ayele, D. Li, Q. Chen, Coupling of alkaline precipitation and alkali-activated hydrogen peroxide oxidation for reuse of cotton pulp black liquor, *J. Clean. Prod.* 288 (2021), 125094.
- [54] S. Zhang, H. Liu, F. Gao, M. Fang, Y. Zhang, Y. Cai, K. Li, M. Kong, X. Tan, The synergetic enhancement of piezo catalytic performance to remove tetracycline by $K_2Ti_6O_{13}/TiO_2$ composite, *J. Alloy. Compd.* 900 (2022), 163492.
- [55] S. Li, Z. Zhao, D. Yu, J.-Z. Zhao, Y. Su, Y. Liu, Y. Lin, W. Liu, H. Xu, Z. Zhang, Few-layer transition metal dichalcogenides (MoS_2 , WS_2 , and WSe_2) for water splitting and degradation of organic pollutants: Understanding the piezocatalytic effect, *Nano Energy* 66 (2019), 104083.
- [56] G. Singh, M. Sharma, R. Vaish, Flexible $Ag@LiNbO_3/PVDF$ Composite Film for Piezocatalytic Dye/Pharmaceutical Degradation and Bacterial Disinfection, *ACS Appl. Mater. Inter.* 13 (2021) 22914–22925.
- [57] Z. Zhuge, X. Liu, T. Chen, Y. Gong, C. Li, L. Niu, S. Xu, X. Xu, Z.A. Allothman, C. Q. Sun, J.G. Shapter, Y. Yamauchi, Highly efficient photocatalytic degradation of different hazardous contaminants by $CaIn_2S_4-Ti_3C_2Tx$ Schottky heterojunction: An experimental and mechanism study, *Chem. Eng. J.* 421 (2021), 127838.
- [58] S. He, C. Yan, X.-Z. Chen, Z. Wang, T. Ouyang, M.-L. Guo, Z.-Q. Liu, Construction of core-shell heterojunction regulating $\alpha-Fe_2O_3$ layer on CeO_2 nanotube arrays enables highly efficient Z-scheme photoelectrocatalysis, *Appl. Catal. B, Environ.* 276 (2020), 119138.
- [59] J. Xiong, X. Li, J. Huang, X. Gao, Z. Chen, J. Liu, H. Li, B. Kang, W. Yao, Y. Zhu, $CN/rGO@BPQDs$ high-low junctions with stretching spatial charge separation ability for photocatalytic degradation and H_2O_2 production, *Appl. Catal. B, Environ.* 266 (2020), 118602.
- [60] Z. Wu, Y. Liang, X. Yuan, D. Zou, J. Fang, L. Jiang, J. Zhang, H. Yang, Z. Xiao, MXene Ti_3C_2 derived Z-scheme photocatalyst of graphene layers anchored $TiO_2/g-C_3N_4$ for visible light photocatalytic degradation of refractory organic pollutants, *Chem. Eng. J.* 394 (2020), 124921.
- [61] M. Zhu, S. Li, H. Zhang, J. Gao, K.W. Kwok, Y. Jia, L.-B. Kong, W. Zhou, B. Peng, Diffused phase transition boosted dye degradation with $Ba(Zr_{x-1}Ti_{1-x})O_3$ solid solutions through piezoelectric effect, *Nano Energy* 89 (2021), 106474.
- [62] A. Zhang, Z. Liu, B. Xie, J. Lu, K. Guo, S. Ke, L. Shu, H. Fan, Vibration catalysis of eco-friendly $Na_0.5K_{0.5}NbO_3$ -based piezoelectric: An efficient phase boundary catalyst, *Appl. Catal. B, Environ.* 279 (2020), 119353.
- [63] L. Chen, Y. Jia, J. Zhao, J. Ma, Z. Wu, G. Yuan, X. Cui, Strong piezocatalysis in barium titanate/carbon hybrid nanocomposites for dye wastewater decomposition, *J. Colloid Interface Sci.* 586 (2021) 758–765.
- [64] Q. Liu, Q. Hu, D. Zhai, Q. Sun, H. Luo, D. Zhang, Superior photo-piezoelectric catalytic performance using $Bi_{0.5}Na_{0.5}TiO_3@BiVO_4$ based cloth, *J. Mater. Chem. A* 9 (2021) 17841–17854.
- [65] L. Xu, C. Wu, P. Liu, X. Bai, X. Du, P. Jin, L. Yang, X. Jin, X. Shi, Y. Wang, Peroxymonosulfate activation by nitrogen-doped biochar from sawdust for the efficient degradation of organic pollutants, *Chem. Eng. J.* 387 (2020), 124065.
- [66] F. Chen, L.L. Liu, J.J. Chen, W.W. Li, Y.P. Chen, Y.J. Zhang, J.H. Wu, S.C. Mei, Q. Yang, H.Q. Yu, Efficient decontamination of organic pollutants under high salinity conditions by a nonradical peroxymonosulfate activation system, *Water Res.* 191 (2021), 116799.
- [67] H. Kan, H. Sokkun, Z. Yang, R. Wu, J. Shen, G. Qu, T. Wang, Purification of dye wastewater using bicarbonate activated hydrogen peroxide: Reaction process and mechanisms, *Sep. Purif. Technol.* 232 (2020), 115974.
- [68] C. Chu, Q. Zhu, Z. Pan, S. Gupta, D. Huang, Y. Du, S. Weon, Y. Wu, C. Muhich, E. Stavitski, K. Domen, J.-H. Kim, Spatially separating redox centers on 2D carbon nitride with cobalt single atom for photocatalytic H_2O_2 production, *Proc. Natl. Acad. Sci.* 117 (2020) 6376–6382.
- [69] C. Fu, G. Sun, C. Wang, B. Wei, G. Ran, Q. Song, Fabrication of nitrogen-doped graphene nanosheets anchored with carbon nanotubes for the degradation of tetracycline in saline water, *Environ. Res.* 206 (2021), 112242.
- [70] C. Fu, G. Sun, G. Yin, C. Wang, G. Ran, Q. Song, P/N co-doped carbon sheet for peroxymonosulfate activation: Edge sites enhanced adsorption and subsequent electron transfer, *Sep. Purif. Technol.* 292 (2022), 120922.
- [71] K. Wang, D. Shao, L. Zhang, Y. Zhou, H. Wang, W. Wang, Efficient piezo-catalytic hydrogen peroxide production from water and oxygen over graphitic carbon nitride, *J. Mater. Chem. A* 7 (2019) 20383–20389.
- [72] J. Yoon, J. Kim, F. Tieves, W. Zhang, M. Alcalde, F. Hollmann, C.B. Park, Piezobiocatalysis: ultrasound-driven enzymatic oxyfunctionalization of C–H bonds, *ACS Catal.* 10 (2020) 5236–5242.
- [73] X. Li, B. Kang, F. Dong, Z. Zhang, X. Luo, L. Han, J. Huang, Z. Feng, Z. Chen, J. Xu, B. Peng, Z.L. Wang, Enhanced photocatalytic degradation and H_2/H_2O_2 production performance of S-pCN/ $WO_{2.72}$ S-scheme heterojunction with appropriate surface oxygen vacancies, *Nano Energy* 81 (2021), 105671.
- [74] Y. Shiraishi, T. Takii, T. Hagi, S. Mori, Y. Kofuji, Y. Kitagawa, S. Tanaka, S. Ichikawa, T. Hirai, Resorcinol-formaldehyde resins as metal-free semiconductor photocatalysts for solar-to-hydrogen peroxide energy conversion, *Nat. Mater.* 18 (2019) 985–993.
- [75] Y. Kofuji, S. Ohkita, Y. Shiraishi, H. Sakamoto, S. Tanaka, S. Ichikawa, T. Hirai, Graphitic carbon nitride doped with biphenyl diimide: efficient photocatalyst for hydrogen peroxide production from water and molecular oxygen by sunlight, *ACS Catal.* 6 (2016) 7021–7029.
- [76] F. Wang, J. Xu, Z. Wang, Y. Lou, C. Pan, Y. Zhu, Unprecedentedly efficient mineralization performance of photocatalysis-self-Fenton system towards organic pollutants over oxygen-doped porous $g-C_3N_4$ nanosheets, *Appl. Catal. B, Environ.* 312 (2022), 121438.
- [77] Y.S. Daiming Liu, Zhijie Xin, Guoxia Liu, Chengchao Jin, Fukai Shan, High-piezocatalytic performance of eco-friendly $(Bi_{1/2}Na_{1/2})TiO_3$ -based nanofibers by electrospinning, *Nano Energy* 65 (2019), 104024.

- [78] L.W. Zhirong Liu, Xin Yu, Jian Zhang, Ruiqi Yang, Xiaodi Zhang, Yanchen Ji, Mengqi Wu, Lin Deng, Linlin Li, Zhong Lin Wang, Piezoelectric-Effect-Enhanced Full-Spectrum Photoelectrocatalysis in p–n Heterojunction, *Adv. Funct. Mater.* 29 (2019), 1807279.
- [79] A.V.-C. Samira Siahrostami, Mohammadreza Karamad, Davide Deiana, Paolo Malacrida, Björn Wickman, María Escudero-Escribano, Elisa A. Paoli, Rasmus Frydendal, Thomas W. Hansen, Ib Chorkendorff, Ifan E.L. Stephens, Jan Rossmeisl, Enabling direct H₂O₂ production through rational electrocatalyst design, *Nat. Mater.* 12 (2013) 1137–1143.
- [80] P.W. Hui Li, Dominique S. Itanze, Zachary D. Hood, Shiba Adhikari, Chang Lu, Xiao Ma, Chaochao Dun, Lin Jiang, David L. Carroll, Yejun Qiu, Scott M. Geyer, Scalable neutral H₂O₂ electrosynthesis by platinum diphosphide nanocrystals by regulating oxygen reduction reaction pathways, *Nat. Commun.* 11 (2020) 3928.